

Equatorial Deep Jets -Modelling and Observation

Master-Arbeit

im **Masterstudiengang (M.Sc.) Climate Physics**
der Mathematisch-Naturwissenschaftlichen Fakultät
der Christian-Albrechts-Universität zu Kiel vorgelegt von

Yao Fu¹

15007

Erstgutachter: Prof. Dr. Richard Greatbatch

Zweitgutachter: Prof. Dr. Peter Brandt

¹*E-mail: yfu@geomar.de*

Abstract

The equatorial deep jets (EDJs) are strong vertically alternating zonal flows extending over almost the full depth of the equatorial oceans. They are trapped in a narrow equatorial band of roughly 1° latitude about the equator, associated with a vertical scale of between 300 m and 700 m; in the Atlantic Ocean, they have a time scale of about 4.5 years. The cross-equatorial width of the EDJs is found to be roughly 1.5 times larger than implied by the linear inviscid theory based on their vertical scale. In this work, EDJs are simulated using a forced, dissipative low-frequency equatorial basin mode in a shallow water model associated with a high-order baroclinic vertical normal mode. The lateral mixing of momentum is found to result in a widening of the simulated EDJs; the widening of the EDJs by the lateral mixing of momentum is considered as one of the explanations of the enhanced cross-equatorial width of the observed EDJs. The zonal velocities measured by the Argo floats are used for comparison of the meridional profiles and the flow strength with the simulations. A value of $300 \text{ m}^2/\text{s}$ for the lateral mixing coefficient is found to be sufficient to account for the observed width of the EDJs; also, the implementation of the background barotropic mean flow leads to a better agreement with the observations at latitudes higher than 2.5° either side of the equator.

Zusammenfassung

Die “equatorial deep Jets” (EDJs) sind stark vertikal alternierend zonalen Strömungen, die sich nahezu über die gesamte Tiefe der äquatorialen Özeane erstrecken. Die meridionale Ausdehnung ist jeweils 1° N/S und die vertikale Ausdehnung variiert zwischen 300 und 700m; im Atlantik haben die EDJs einer Zeitskala von etwa 4,5 Jahren. Die meridionale Breite der EDJs ist ungefähr 1,5 mal größer als die von linearer reibungsfreier Theorie impliziert wird. In dieser Arbeit werden die EDJs mithilfe eines “shallow water models” simuliert und können als ein “forced, dissipative low-frequency basin mode” mit einem “high-order baroclinic vertical normal mode” dargestellt werden. Es wird herausgefunden, dass die “lateral mixing of momentum” zu einer meridionalen Ausdehnung der simulierten EDJs führt; die Ausdehnung durch “lateral mixing of momentum” wird als eine der Ursachen der vergrößerten meridionalen Breite betrachtet. Die aus Argo Float Daten abgeleiteten zonalen Geschwindigkeiten sind für Vergleich mit den Simulationen verwendet. Mit “lateral mixing coefficient” von $300 \text{ m}^2/\text{s}$ zeigt das Modell gute Übereinstimmung mit Messungen bezüglich der meridionalen Breite der EDJs; zudem verbessert die Umsetzung der hintergründig barotropen mittleren Strömung die Ergebnisse der Modellsimulationen, insbesondere bei Breitengraden höheren als $2,5^\circ$ auf beiden Seiten des Äquators.

Contents

1	Introduction	5
1.1	Equatorial Deep Jets	5
1.2	Vertical Normal Modes	7
1.3	Equatorial Basin Modes	10
1.4	Lateral Mixing of Momentum	10
2	Model and Data	12
2.1	The Shallow Water Model	12
2.1.1	Experiment without Mean Flow	12
2.1.2	Experiment with Mean Flow	14
2.2	Observational Data	18
3	Results	22
3.1	Model Results	22
3.1.1	Model Simulation without Background Mean Flow	22
3.1.2	Model Simulation with Background Mean Flow	35
3.2	Comparison with Observation	41
3.2.1	Profile Comparison	41
3.2.2	Root Mean Square Comparison	47
4	Summary and Discussion	54
5	Acknowledgement	57

1 Introduction

1.1 Equatorial Deep Jets

In the past few decades, Equatorial Deep Jets (EDJs) have been confirmed by observations as a ubiquitous feature along the equator of all three oceans. The jets were first discovered by [Luyten and Swallow \(1976\)](#) in the equatorial Indian Ocean from full-depth current profiles. The existence of such jets in the Pacific Ocean was then reported by [Hayes and Milburn \(1980\)](#), [Leetmaa and Spain \(1981\)](#) and [Eriksen \(1981\)](#). In the Atlantic ocean, the presence of the jets was first inferred by [Eriksen \(1982\)](#) from hydrographic data, and then confirmed by [Ponte and Luyten \(1990\)](#) from direct current measurements.

Observations in all three oceans have revealed similar characteristics of the EDJs. They are deep zonal currents that alternate their direction vertically, extending from beneath the Equatorial Undercurrent (EUC) down to at least 3000 m (cf. Fig. 1b of [Eden and Dengler \(2008\)](#)). These flows are trapped within a narrow equatorial band of approximately 1° latitude about the equator with amplitudes up to 20 *cm/s* and vertical scale in hundreds of meters.

In the Atlantic Ocean, a periodic behaviour of the EDJs has been noted by many authors. [Johnson and Zhang \(2003\)](#) estimated a 5 ± 1 *yr* period for the EDJs calculated from available deep CTD stations. [Bunge et al. \(2008\)](#) and [Brandt et al. \(2011\)](#) reported a roughly 4.5 *yr* period by fitting a plane wave to moored ADCP data at $23^\circ W$ and Argo float data (see Fig. 2.3 discussed later), respectively. A downward phase propagation of about 100 *m/yr* has also been noted in these papers. This, according to linear internal wave theory, is related to upward energy propagation, which implies a deep generation mechanism for EDJs ([Brandt et al., 2011](#)). However, the meridional scale of EDJs is found to be 1.5 times larger than implied by their vertical scale based on inviscid, linear theory ([Johnson and Zhang, 2003](#)); a similar feature is also found in the equatorial Pacific Ocean ([Muench et al., 1994](#)).

Fig. 1.1a, an update from Fig. 5 of [Brandt et al. \(2012\)](#), shows the zonal velocity obtained from moored observations at $23^\circ W$ at the equator. Apart from the EUC in the surface layer, a deep jet signal with eastward and westward velocities and downward phase propagation between 200 m and 700 m can be clearly detected. A harmonic fit to the same data in the depth range of 250 - 600 m using a period of 1670 days (Fig. 1.1b) reveals the structure of the observed EDJs, confirming their periodicity and the downward phase propagation. An interesting feature of the harmonic fit amplitude is that at about 400-m depth, a minimum occurs, which may be

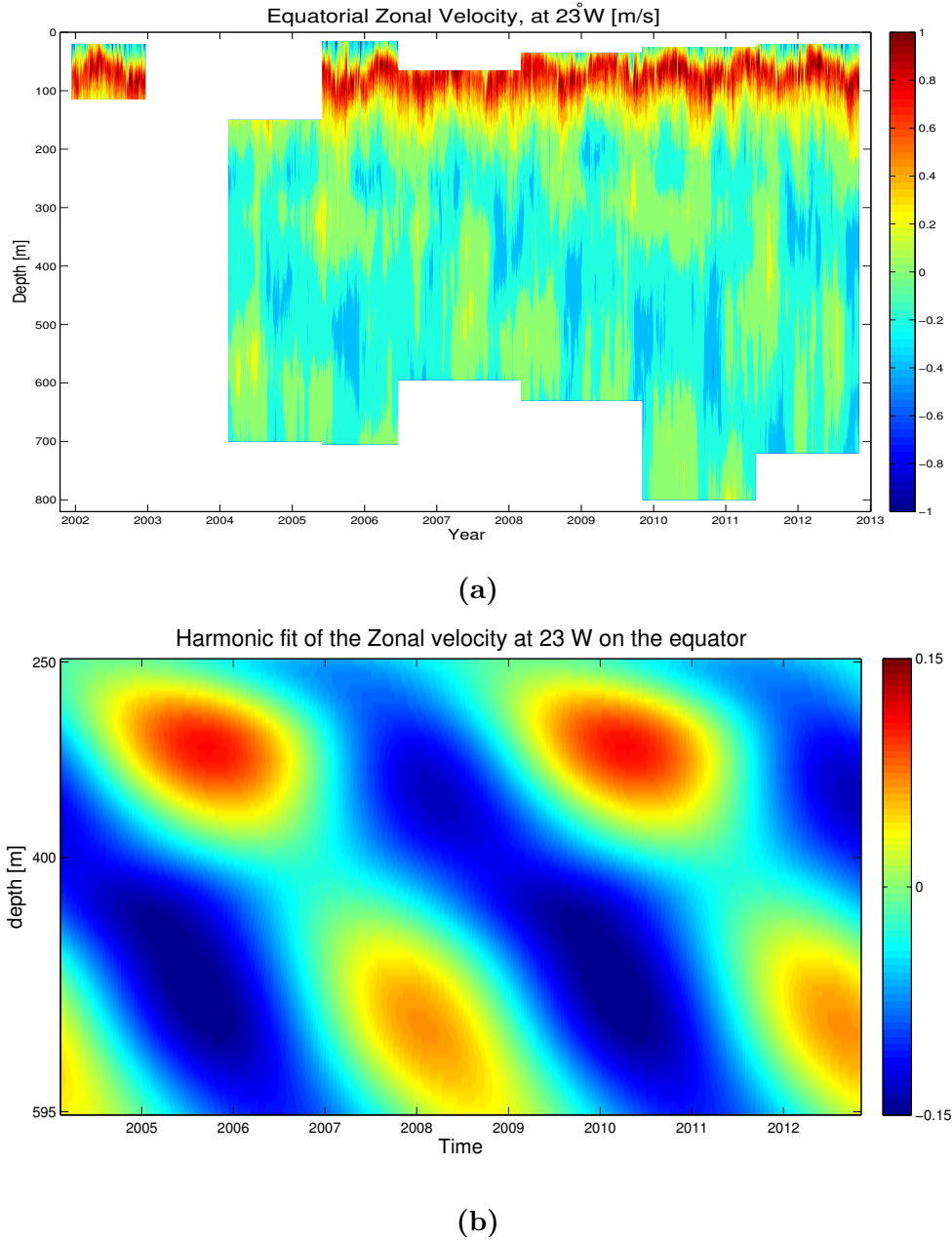


Figure. 1.1 | (a) Zonal velocity from moored ADCP data at 23°W at the equator similar to Fig. 5 of *Brandt et al. (2012)*. The data have been updated using the newly recovered moored ADCP data from cruise MSM22. (b) Harmonic fit of the same zonal velocity between 250 and 600 m, using a period of 1670 days. Note that the depth range plotted in (b) is different from that in (a).

due to a superposition of equatorial waves at this depth.

Eden and Dengler (2008) conducted a simulation of Atlantic EDJs using four different versions of a general circulation model, which differ in their horizontal and vertical resolution. Two of them have an identical horizontal resolution of $1/3^\circ$ but 45 and 450 vertical levels,

respectively; while the other two have an higher identical horizontal resolution of $1/12^\circ$ but 45 and 94 vertical levels, respectively. All the simulations mimic an EDJ-like structure at $35^\circ W$ at the equator. The best representation happens in the model with $1/12^\circ$ horizontal resolution and 94 vertical levels. A clear improvement can be already seen in the model with $1/3^\circ$ horizontal resolution and 450 vertical levels compared to those model runs with 45 vertical levels. However, even their best simulation reproduced neither the observed strength of Atlantic EDJs nor the enhanced energy observed at $2 - 2.5^\circ$ away from the equator.

[Hua et al. \(1997\)](#) proposed a symmetric instability theory to explain the generation mechanism of EDJs, which suggests that a shear instability caused by the large scale flow field at the equator could trigger the deep jets. [Eden and Dengler \(2008\)](#) also tested the symmetric instability theory in their model simulation. They noted that a zonally constant zonal mean flow has to be assumed, which is quite unrealistic compared with the complications in the real world, and they concluded that it is unlikely that symmetric instability plays a dominant role for the generation of deep jets in reality. [D'Orgeville et al. \(2007\)](#), [Hua et al. \(2008\)](#), and [Fruman et al. \(2009\)](#) have proposed that barotropic destabilization of mixed Rossby-gravity waves with short zonal wavelength and low baroclinic vertical mode in the western boundary region of the equatorial oceans could transfer energy to long Kelvin waves of a high baroclinic mode, this is a more likely explanation.

It is reported that in the tropical Atlantic, the sea surface climate can be affected by the EDJs ([Brandt et al., 2011](#)). A 4.5-yr climate cycle that coincides with the period of Atlantic EDJs has been identified for sea surface temperature, wind and precipitation in the tropical Atlantic (Fig. 1b of [Brandt et al. \(2011\)](#)), and which is related to the upward energy propagation of EDJs mentioned above. Moreover, a close relation between the observed oxygen variability at depth in the equatorial Atlantic and EDJs has been found by [Brandt et al. \(2012\)](#), together with an implied eastward oxygen flux associated with the EDJs, contributing to maintain the oxygen-rich equatorial region between the two oxygen minimum zones of both hemispheres. Regarding the importance of the equatorial deep jets to the tropical Atlantic climate, more explorations must be made to deepen the understanding of EDJs.

1.2 Vertical Normal Modes

Since the Atlantic EDJs are the concern of this work, and a shallow water model is used to simulate some horizontal features of the EDJs, the concept of baroclinic vertical normal

modes and low-frequency equatorial basin modes must be introduced first in order to make the connection between the shallow water model and the equatorial deep jets.

For a continuously stratified ocean with flat bottom whose horizontal extent is much larger than its vertical extent, certain simplifications can be made and a separation of variables technique can be applied. The result of this method is that the variables describing the ocean can be expressed as a sum of an infinite set of modes, each of which consists of the product of the vertical structure function and its corresponding horizontal structure function (*Gill, 1982; Gill and Clarke, 1974*). Taking zonal and vertical velocity u and w on the Cartesian coordinates as an example, we can write

$$u(x, y, z, t) = \sum_{n=1}^{\infty} \tilde{u}_n(x, y, t) \hat{p}_n(z) \quad (1)$$

$$w(x, y, z, t) = \sum_{n=1}^{\infty} \tilde{w}_n(x, y, t) \hat{w}_n(z) \quad (2)$$

where the notation \tilde{u}_n and \tilde{w}_n represent the horizontal structure function, and \hat{p}_n and \hat{w}_n represent the vertical structure function, respectively; $n = 0, 1, 2, \dots$ etc denotes the n^{th} vertical normal mode.

The vertical structure functions $\hat{p}_n(z)$ and $\hat{w}_n(z)$ satisfy the differential equations in Sturm-Liouville form:

$$\frac{d}{dz} \left[\frac{1}{N^2} \frac{d\hat{p}_n}{dz} \right] + \frac{1}{c_n^2} \hat{p}_n = 0 \quad (3)$$

$$\frac{d^2 \hat{w}_n}{dz^2} + \frac{N^2}{c_n^2} \hat{w}_n = 0 \quad (4)$$

with boundary conditions:

$$\hat{w}_n(z) = 0 \quad \text{and} \quad \frac{1}{N^2} \frac{d\hat{p}_n(z)}{dz} = 0 \quad \text{at } z = 0 \text{ (the ocean surface)} \quad (5)$$

and

$$\hat{w}_n(z) = 0 \quad \text{and} \quad \frac{1}{N^2} \frac{d\hat{p}_n(z)}{dz} = 0 \quad \text{at } z = -H \text{ (the ocean bottom)} \quad (6)$$

The solutions of Eq. 3 and Eq. 4 are

$$\hat{p}_n(z) = A_n \cos\left(\frac{n\pi z}{H}\right) \quad (7)$$

$$\hat{w}_n(z) = B_n \sin\left(\frac{n\pi z}{H}\right) \quad (8)$$

with a separation constant $c_n = \frac{NH}{n\pi}$, where $N^2 = -\rho_0^{-1} g \frac{d\bar{\rho}}{dz}$ is the buoyancy frequency, H is the total water depth, ρ_0 is a typical water density. Note that N^2 in this case is a constant profile

since a uniform stratification is assumed. A_n and B_n are constants. Here c_n is also the phase velocity of the equatorial Kelvin waves that will be mentioned later on.

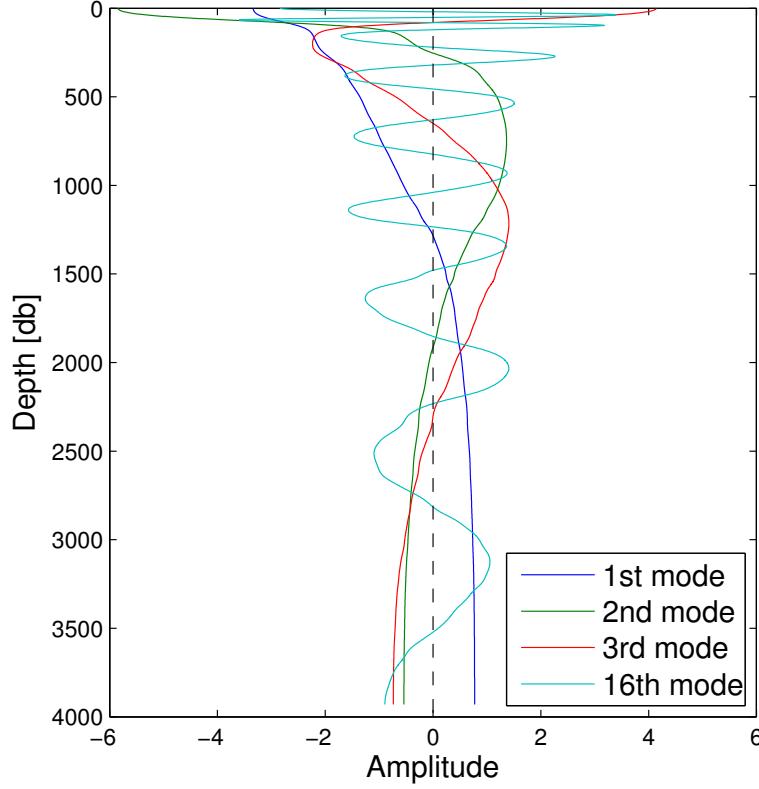


Figure. 1.2 | Vertical structure of the first three and the 16th vertical modes calculated from the mean CTD profile at 23°W at the equator. Note that in this example, N^2 is also calculated from observations, so it varies vertically.

Fig. 1.2 illustrates the vertical structure of the first three and 16th vertical mode computed from the mean CTD profile at 23°W at the equator computed from cruise data. $\hat{p}_1(z)$ has 1 zero-crossing, $\hat{p}_2(z)$ has 2 zero-crossings, and $\hat{p}_n(z)$ has n zero-crossings. The phase velocity decreases with n . In this example, $c_1 \approx 2.40$ m/s, $c_3 \approx 0.93$ m/s, and $c_{16} \approx 0.17$ m/s.

Note that the modes are orthogonal to each other, indicating that each mode is statistically independent of any other mode. Also, for each normal mode, the horizontal structure satisfies the linear shallow water equations in the following form,

$$\tilde{u}_{nt} - f\tilde{v}_n = -g\tilde{\eta}_{nx} \quad (9)$$

$$\tilde{v}_{nt} + f\tilde{u}_n = -g\tilde{\eta}_{ny} \quad (10)$$

$$\tilde{\eta}_{nt} + H_n(\tilde{u}_{nx} + \tilde{v}_{ny}) = 0 \quad (11)$$

where $c_n = \sqrt{gH_n}$ is the separation constant of the n^{th} mode and also the corresponding gravity wave speed, $\tilde{\eta}_{nt}$ represents the isopycnal displacement, and H_n is the equivalent depth. Note that c_n for each mode is given by $c_n = \frac{NH}{n\pi}$. Also, for a given normal mode of interest, the equivalent depth H_n can be computed from $H_n = c_n^2/g$. The shallow water equations given above govern the horizontal behaviour of the associated normal mode.

1.3 Equatorial Basin Modes

A low-frequency basin mode, in the limit of the long-wave approximation, on a meridionally infinite equatorial beta plane, is described by [Cane and Moore \(1981\)](#), and consists of an eastward propagating equatorial Kelvin wave and a reflected westward propagating long Rossby wave. The correspondence between EDJs and this gravest equatorial basin mode for a high order baroclinic normal mode has been mentioned by several authors. For example, [Johnson and Zhang \(2003\)](#) discussed the similarity between the EDJs and the first-meridional-mode equatorial Rossby wave; [D’Orgeville et al. \(2007\)](#) discussed the correspondence of the oscillating period of the EDJs and the first equatorial basin mode; [Brandt et al. \(2011\)](#) pointed out the consistency between Atlantic EDJs and high order baroclinic basin modes.

The low-frequency basin mode for a given baroclinic normal mode with separation constant c_n can be understood as a Kelvin wave propagating eastward with phase velocity c_n across the basin of width L_e , and being reflected at the eastern boundary as a first-meridional-mode long Rossby wave, which propagates towards the western boundary with phase velocity $\frac{c_n}{3}$ and is reflected as a Kelvin wave in the next cycle and so on. Therefore the period of one complete cycle is $\frac{4L_e}{c_n}$. The 1670 days period of Atlantic EDJs mentioned above corresponds to a phase velocity of 0.17 m/s , associated with about the 15^{th} vertical normal mode (cf. Fig. 11 in [Brandt et al. \(2008\)](#)). In the research of [Brandt et al. \(2008\)](#) a set of vertical structure functions was fitted to the detrended moored zonal velocity data at $23^\circ W$ at the equator. The resulting vertical mode spectrum gives a distinct peak at the 15th mode, indicating that the Atlantic EDJ are closely related to the 15th baroclinic vertical normal mode.

1.4 Lateral Mixing of Momentum

In the simulation of the Atlantic EDJs with a shallow water model, we primarily examine the dependence of the meridional width about the equator, and the amplitude of the zonal velocity, on the specified lateral mixing of momentum. [Yamagata and Philander \(1985\)](#) have

discussed the underlying physics. For a baroclinic equatorial basin mode, the zonal current along the equator is approximately in geostrophic balance. The strength of the zonal flow is then determined by the meridional density gradient either side of the equator by the thermal wind equations. Therefore a reduction of the flow strength along the equator resulting from a momentum flux into the adjacent areas leads to a decrease of the meridional density gradient. However, below the region where the EUC generates strong vertical shear, diapycnal mixing is extremely weak ([Dengler and Quadfasel, 2002](#)), with typical diapycnal diffusivities of order $10^{-6} m^2/s$. It follows that diapycnal mixing is not responsible for reducing the meridional density gradients, hence a greater meridional width is required to reduce the meridional density gradient. ([Greatbatch et al., 2012](#)). Moreover, [Brandt et al. \(2008\)](#) suggested that a lateral mixing coefficient of $400 m^2/s$ is enough to account for the reducing oxygen concentration from west to east in the core of the oxygen tongue along the equator.

The shallow water model used in this work and the observational data for comparison with the model, are described in the following chapter. In Chapter 3 the results from the model simulation and the comparison with the observations will be made. Finally, a summary and discussion of our conclusions will be presented in the last chapter.

2 Model and Data

2.1 The Shallow Water Model

Our work is based on a shallow water model, with which the horizontal structure of the Atlantic EDJs associated with a high-order baroclinic vertical normal mode is simulated. We idealize the tropical Atlantic as an rectangular basin with a flat bottom, whose zonal extent is 55° longitude similar to that in reality, and meridional extent is from $10^\circ S$ to $10^\circ N$. Apart from the resonant forcing that is applied to counter the dissipation, the bottom friction and Newtonian cooling terms are switched off, allowing us to examine the direct influence of the lateral mixing of momentum on the horizontal behaviour of the EDJs. As to be shown in the following chapters, two scenarios of experiments are carried out. The first consists of model simulation without the background mean flow; the second includes the background mean flow.

2.1.1 Experiment without Mean Flow

2.1.1.1 Basic Equations

The governing equations for a given baroclinic vertical normal mode in spherical coordinates (cf. [Greatbatch et al. \(2012\)](#)) are

$$u_t - fv = -\frac{g}{a \cos \theta} \frac{\partial \eta}{\partial \lambda} + X + F^u \quad (12)$$

$$v_t + fu = -\frac{g}{a} \frac{\partial \eta}{\partial \theta} + F^v \quad (13)$$

$$\eta_t + \frac{H_e}{a \cos \theta} \left[\frac{\partial u}{\partial \lambda} + \frac{\partial (\cos \theta v)}{\partial \theta} \right] = 0 \quad (14)$$

where u and v are horizontal velocity components in the eastward and northward direction, respectively; a is the radius of the earth; θ and λ represent latitude and longitude, respectively; $f = 2\Omega \sin \theta$ is the Coriolis parameter, in which $\Omega = 7.27 \times 10^{-5} \text{ rad/s}$ is the angular velocity of the Earth's rotation; $g = 9.8 \text{ m/s}^2$ is the gravity acceleration; η is the isopycnal displacement; X represents the forcing required to balance the dissipation; F^u and F^v are the lateral mixing of momentum with eddy viscosity A_h ; and $H_e = 2.93 \times 10^{-3} \text{ m}$ is the equivalent depth. As discussed above, this value of H_e corresponds to $c_n \approx 0.17 \text{ m/s}$, associated with a equatorial basin mode period $T_B = 1670 \text{ days}$ for the Atlantic Ocean.

2.1.1.2 Lateral Mixing of Momentum

The lateral mixing of momentum is given by

$$F^u = A_h f^\lambda \quad (15)$$

in the zonal direction, and

$$F^v = A_h f^\theta \quad (16)$$

in the meridional direction, where A_h is the horizontal eddy viscosity. The lateral mixing of momentum is parameterized in spherical coordinates in the form of conservation of momentum by

$$f^\lambda = \nabla^2 u + \frac{u(1 - \tan^2 \theta)}{a^2} - \frac{2 \sin \theta}{a^2 \cos^2 \theta} \frac{\partial v}{\partial \lambda} \quad (17)$$

$$f^\theta = \nabla^2 v + \frac{v(1 - \tan^2 \theta)}{a^2} + \frac{2 \sin \theta}{a^2 \cos^2 \theta} \frac{\partial u}{\partial \lambda} \quad (18)$$

and ∇^2 is the Laplacian operator given by

$$\nabla^2 Q^* = \left[\frac{1}{a^2 \cos^2 \theta} \frac{\partial^2 Q^*}{\partial \lambda^2} + \frac{1}{a^2 \cos \theta} \frac{\partial}{\partial \theta} \left(\cos \theta \frac{\partial Q^*}{\partial \theta} \right) \right] \quad (19)$$

2.1.1.3 Forcing

To counter the dissipation resulting from the lateral mixing of momentum, an oscillatory forcing is applied in the zonal momentum equation Eq. 12, which is generally given by

$$X = X_0 \sin(\omega t) \quad (20)$$

where $\omega = 2\pi/T_B$ is the angular frequency, T_B is the gravest equatorial basin mode period (see Fig. 3.3 later for discussion of the resonance of the forcing with a basin mode), and X_0 is an arbitrary amplitude. Because we are interested in the influence of the position of the forcing on the horizontal structure of the Atlantic EDJs, the forcing is confined in specific regions in different experiments, namely “full”, “centre”, “west”, “east”, and “equator”. For the “full” case, the forcing is applied zonally uniformly over the full basin with a uniform amplitude X_0 , and $T_B = 1.44288 \times 10^8$ s (corresponding to 1670 days). For the case “centre”, “west”, and “east”, the forcing is confined over the central third, western third and eastern third of the basin with exactly the same X_0 and T_B as in the case “full”, respectively. For the case “equator”, the forcing is given by

$$X = X_0 e^{-(\beta y^2/2c)} \sin(\omega t) \quad (21)$$

where $y = a\theta$ (θ in radians); $\beta = 2\Omega/a = 2.3 \times 10^{-11} \text{ m}^{-1}\text{s}^{-1}$ and hence the forcing is still zonally uniform but confined within an equatorial Rossby radius of deformation of the equator with the same T_B and X_0 used in the former experiments.

2.1.1.4 Boundary Conditions

A free slip boundary condition is applied to the lateral viscosity term on all the boundaries. This means that at the boundaries, the velocity normal to the boundaries is zero, i.e. $u = 0$ at eastern-western boundaries and $v = 0$ at northern-southern boundaries; and the gradient of the velocity parallel to the boundaries is zero, i.e. $v_\lambda = 0$ at eastern-western boundaries and $u_\theta = 0$ at northern-southern boundaries. On the northern-southern boundaries sponge layers are used to eliminate Kelvin wave propagation along these boundaries ([Yang and Liu, 2003](#)), the sponge layers can be understood as a damping term added to η in the continuity equation (Eq. 14). It functions only in the boundary layers to damp wave propagation there.

For each experiment in this scenario, a horizontal eddy viscosity A_h and wind forcing X are specified, the model is forced by the wind forcing to a steady oscillatory state, and a Arakawa C-grid is used here as a natural way of finite differencing.

2.1.2 Experiment with Mean Flow

2.1.2.1 Basic Equations

The shallow water equations for a baroclinic mode including the barotropic mean flow (U, V) in spherical coordinates are

$$u_t - (f + ROT)v - \zeta V = -\frac{1}{a\cos\theta} \frac{\partial(g\eta + E)}{\partial\lambda} + X + F^u \quad (22)$$

$$v_t + (f + ROT)u + \zeta U = -\frac{1}{a} \frac{\partial(g\eta + E)}{\partial\theta} + F^v \quad (23)$$

$$\eta_t + \frac{H}{a\cos\theta} \left[\frac{\partial u}{\partial\lambda} + \frac{\partial(\cos\theta v)}{\partial\theta} \right] + \frac{1}{a\cos\theta} \left[\frac{\partial(U\eta)}{\partial\lambda} + \frac{\partial(\cos\theta V\eta)}{\partial\theta} \right] = 0 \quad (24)$$

where the mean flow (U, V) satisfies

$$\frac{1}{a\cos\theta} \left[\frac{\partial U}{\partial\lambda} + \frac{\partial(\cos\theta V)}{\partial\theta} \right] = 0, \quad (25)$$

where (U, V) are defined by a streamfunction as

$$U = -\frac{1}{a} \frac{\partial\psi}{\partial\theta}, \text{ and} \quad (26)$$

$$V = \frac{1}{a \cos \theta} \frac{\partial \psi}{\partial \lambda} \quad (27)$$

and are calculated by centred differencing from ψ (Fig. 2.2).

Also, in the basic equations the term ROT represents the relative vorticity of the mean flow, given by

$$ROT = \frac{1}{a \cos \theta} \left[\frac{\partial V}{\partial \lambda} - \frac{\partial (\cos \theta U)}{\partial \theta} \right], \quad (28)$$

ζ represents the relative vorticity of the perturbations about the mean flow, given by

$$\zeta = \frac{1}{a \cos \theta} \left[\frac{\partial v}{\partial \lambda} - \frac{\partial (\cos \theta u)}{\partial \theta} \right] \quad (29)$$

and E represents the perturbed part of the kinetic energy, given by

$$E = uU + vV \quad (30)$$

2.1.2.2 Barotropic Mean Flow

The barotropic mean flow is calculated using the zonal velocity obtained from 24 cruises along $23^\circ W$, listed in Table 1. To calculate the stream function of the mean flow, we first take the zonal velocities below 300 meters to avoid the influence of the strong currents in the upper ocean, such as EUC. We average the zonal velocity over all the cruises and over the depth, giving a mean profile of the zonal velocity between $5^\circ S$ and $5^\circ N$ along $23^\circ W$. Then the mean of the zonal velocity is removed in order to prevent any net transport by the mean flow in that latitude range. The stream function ψ of the mean flow is obtained by integrating Eq. 26 with latitude. Afterwards, the stream function is multiplied by a zonal structure function Eq. 31, giving ψ a longitudinal dependence. The zonal dependence function is given by

$$plat = \frac{1}{2} \tanh(\alpha_x(x - x_W - x_0)) - \frac{1}{2} \tanh(\alpha_x(x - x_E + x_0)) \quad (31)$$

where \tanh is the hyperbolic tangent function; $\alpha_x = 0.855$ is a stretching factor that determines the slope of the transition zone (see caption of Fig. 2.1), x represents longitude, x_E and x_W are the location of eastern and western boundary, respectively; $x_0 = 3.5^\circ$ latitude is the distance from the centres (red dots in the upper plot of Fig. 2.1) of the transition zones to the eastern and western boundaries. Doing so gives a stream function that is zonally uniform between the two transition zones. The stream function decays to zero within the transition zones and is zero at the boundaries (lower plot in Fig. 2.1).

table. 1 | List of the cruises used to calculate the mean velocity section at $23^\circ W$ for the calculation of the mean flow.

Cruise	section	Max depth (m)
Thalassa (Aug 1999)	$6^\circ S - 6^\circ N, 23^\circ W$	6000
Seward Johnson (Jan 2000)	$6^\circ S - 4^\circ N, 23^\circ W$	2000
Meteor 47/1 (Apr 2000)	$5^\circ S - 4^\circ N, 23^\circ W$	5000
Meteor 55 (Oct 2002)	$0^\circ - 10^\circ N, 24^\circ W$	650
Polarstern ANT XXII/5 (June 2005)	$20^\circ S - 20^\circ N, 23^\circ W$	300
Meteor 68/1 (May 2006)	$2^\circ S - 0.5^\circ N, 23^\circ W$	500
Ron Brown (June 2006)	$5^\circ S - 13.5^\circ N, 23^\circ W$	1500
Meteor 68/2 (JuneJuly 2006)	$4^\circ S - 15.25^\circ N, 23^\circ W$	1300
Ron Brown (JuneJuly 2006)	$5^\circ - 14.5^\circ N, 23^\circ W$	1500
Ron Brown (May 2007)	$4^\circ - 15.5^\circ N, 23^\circ W$	1500
Maria S. Merian 08/1 (Apr. 2008)	$7.5^\circ - 14^\circ N, 23^\circ W$	600
LAtalante (FebMar 2008)	$2^\circ S - 14^\circ N, 23^\circ W$	400
LAtalante (Mar 2008)	$2^\circ S - 14^\circ N, 23^\circ W$	1300
Maria S Merian 10/1 (NovDec) 2008	$4^\circ - 14^\circ N, 23^\circ W$	1000
Polarstern ANT XXV/5 (AprMay 2009)	$20^\circ S - 20^\circ N, 23^\circ W$	250
Endeavour 463 (May 2009)	$5^\circ S - 3^\circ N, 23^\circ W$	725
Meteor 80/1 (OctNov 2009)	$6^\circ S - 15^\circ N, 23^\circ W$	600
Polarstern ANT XXVI/1 (OctNov 2009)	$20^\circ S - 20^\circ N, 23^\circ W$	250
Meteor 80/1 (Nov 2009)	$6^\circ S - 15^\circ N, 23^\circ W$	4500
Meteor 81/1 (Feb 2010)	$11.5^\circ S - 13^\circ N, 22^\circ W$	1200
Polarstern ANT XXVI/4 (AprMay 2010)	$5^\circ S - 13.5^\circ N, 23^\circ W$	250
Maria S. Merian 18/2 (May 2011)	$0^\circ - 4^\circ N, 23^\circ W$	2000
Maria S. Merian 18/2 (MayJune 2011)	$5^\circ S - 5^\circ N, 23^\circ W$	5200

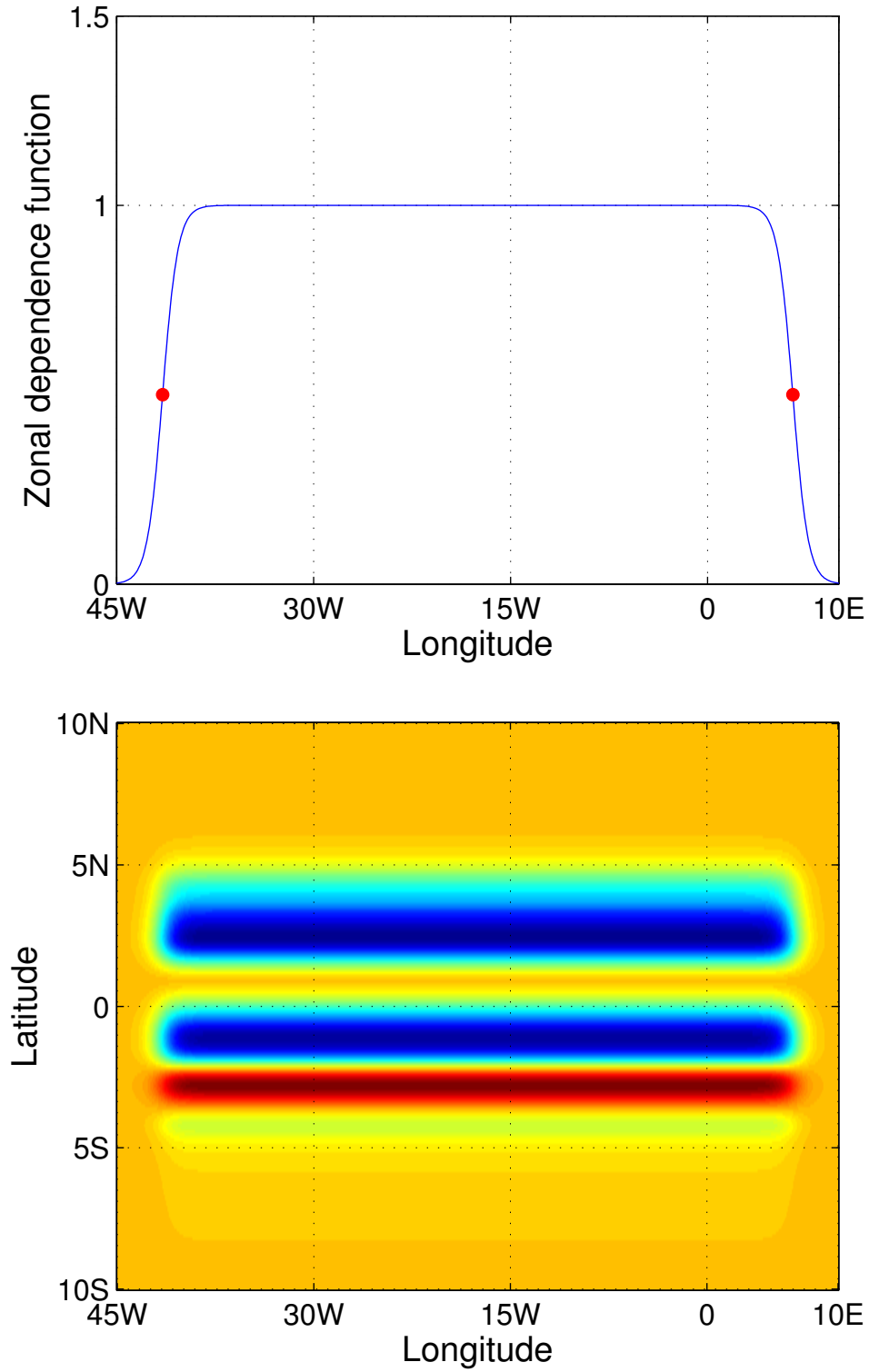


Figure. 2.1 | The zonal structure function (Eq. 31) (upper panel). The stream function of the barotropic mean flow (lower panel). In the upper panel, the two steep branches with red dots near the western and eastern boundaries are the transition zones given by the hyperbolic tangent function; the red dots are the centres of the transition zones.

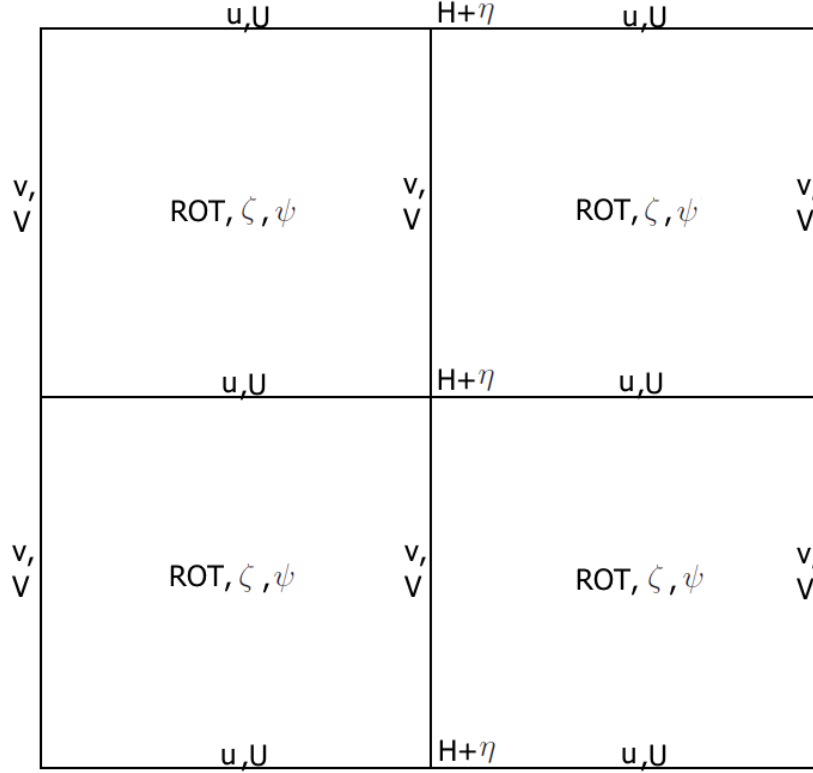


Figure. 2.2 | The staggered grid for the finite-differencing in the experiment with mean flow.

The barotropic mean flow is added to the shallow water equations. We then force the model with the same oscillatory forcing and note the effect of the mean flow. Following [Sadourny \(1975\)](#), a grid illustrated in Fig. 2.2 is used in the simulation with mean flow. The other conditions and setup of the model simulations are identical as in the model setup without mean flow. As before, we test the model solution using different specifications of A_h and forcing X .

In both scenarios, a two-level Adams-Bashforth scheme is applied to integrate the equations, except that the sponge layers (see 2.1.1.4 about sponge layers) are integrated implicitly; the other terms are integrated explicitly. The horizontal resolution for both scenarios is 0.1° . To satisfy the CFL criterion (i.e. $\frac{c\Delta t}{\Delta x} < 1$) and keep the model stable in time, time steps $\Delta t = 2.88576 \times 10^4 \text{ s}$ and $\Delta t^{MF} = 0.96192 \times 10^4 \text{ s}$ are applied in the scenario without mean flow and with mean flow, respectively.

2.2 Observational Data

To compare the horizontal structure of the simulated Atlantic EDJs with observational data, the YoMaHa'07 dataset is used, which contains estimates of velocities of deep and surface currents

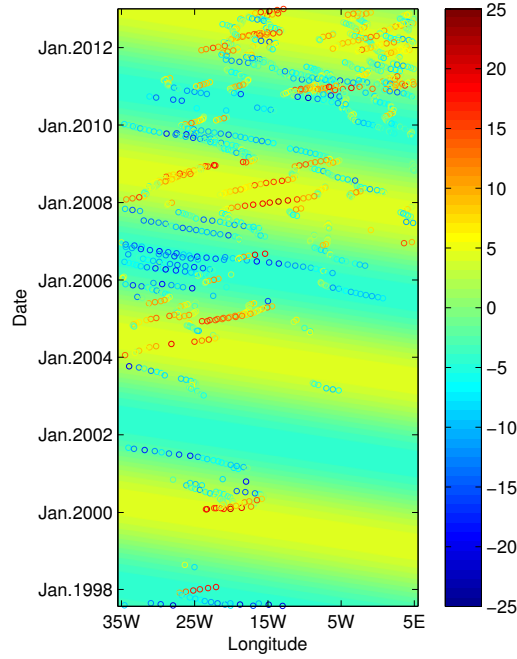


Figure. 2.3 | Equatorial zonal velocities from 1000-dbar Argo float data. This is a redraw of Fig. 4 in [Brandt et al. \(2011\)](#) using updated data. The velocity data (coloured dots) were obtained between $1^{\circ}S$ and $1^{\circ}N$. The colour shading represents the dominant interannual variability in the equatorial Atlantic achieved by a plane-wave fit through maximizing the explained variance.

obtained using data derived from the trajectories of Argo floats. The first measurement was on August 04, 1997 and the data are updated monthly. Argo floats are designed to measure the velocities at their parking depth and make CTD profiles on their way to and from the surface. The collected data are transmitted to ARGOS satellites when the floats are at the sea surface. Each saved data point includes the information about longitude, latitude, depth, Julian time, zonal velocity, meridional velocity and the error estimates of the velocities. The unit of the velocities is cm/s . A detailed description of YoMaHa'07 dataset can be found in [Lebedev et al. \(2007\)](#).

Since we are interested in the horizontal structure of the deep jets, only the zonal velocities measured by the Argo floats, whose parking depth is 1000 *dbar*, were extracted. The missing values and the velocities with an error estimate greater than 2 cm/s , as well as the velocities greater than 4 times of the standard deviation from the mean zonal velocity at 1000 *dbar* depth, have been excluded to filter the outliers. A choice of region is then made based on the availability of Argo float data. Fig. 2.3 is an updated version of Fig. 4 in [Brandt et al. \(2011\)](#).

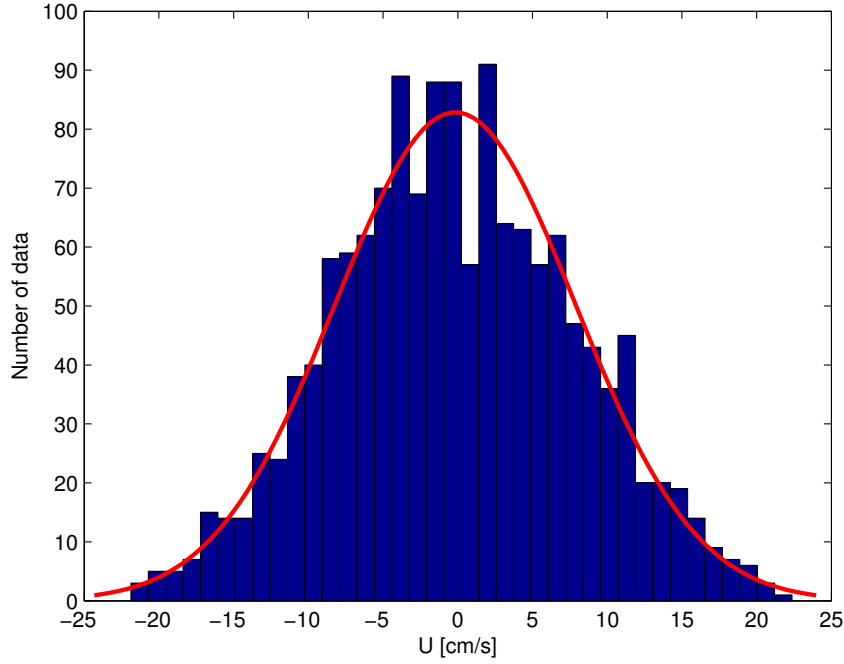


Figure. 2.4 | Histogram of zonal velocity in the equatorial band (between $1^{\circ}S$ and $1^{\circ}N$). The estimated normal probability density function is drawn in red curve. Note that 38 bins are used here, the number of bins is the square root of the number of available data. Note that the normal density function is generated by using the parameters estimated from the data.

The coloured dots show that in the tropical Atlantic (between $1^{\circ}S$ and $1^{\circ}N$) zonal velocities from Argo floats at 1000-dbar depth are mostly available between $35^{\circ}W$ and $15^{\circ}W$ throughout the whole time. A plane wave fit obtained by maximizing the explained variance reveals a harmonic period of 1563 *days* (corresponding approximately to a basin mode period for the 15th baroclinic mode) with a wavelength of about 16.4×10^3 *km* and an explained variance of about 15.7%. This explained variance is only slightly more than a half of the value in [Brandt et al. \(2011\)](#), and may have resulted from the variations in the newly updated data. Though in the newly updated data, the measurement location tends towards the eastern half of the basin, most available data throughout the entire time shown in Fig. 2.3 are between $35^{\circ}W$ and $15^{\circ}W$. Hence, we limit the application of data in the region between $35^{\circ}W$ and $15^{\circ}W$ and $5^{\circ}S$ and $5^{\circ}N$.

Fig. 2.4 is the histogram of the zonal velocity data between $1^{\circ}S$ and $1^{\circ}N$. 38 bins are used and the number of bins is the square root of the number of available data. The red curve is the estimated normal density function. The zonal velocity measured by Argo floats between $1^{\circ}S$ and $1^{\circ}N$ are roughly in a normal distribution with the mean close to -0.17 *cm/s* and standard

deviation of about 8.05 cm/s . 95% of the data lie between -15.8 and 15.8 cm/s .

3 Results

3.1 Model Results

3.1.1 Model Simulation without Background Mean Flow

Prior to the equatorial deep jets simulation, a unforced equatorial low-frequency basin mode described above has been set up. The initial conditions for this test follows the analytic solution of *Cane and Moore (1981)*:

$$[u, v, \eta] = [-itan2s, i\omega y(sec2s)^2, 1] \times \sqrt{\cos2s} e^{i\frac{y^2}{2}\tan2s} \quad (32)$$

where i is the imaginary unit, ω is the frequency, $s = \omega(x - X_e)$, and X_e is the basin width.

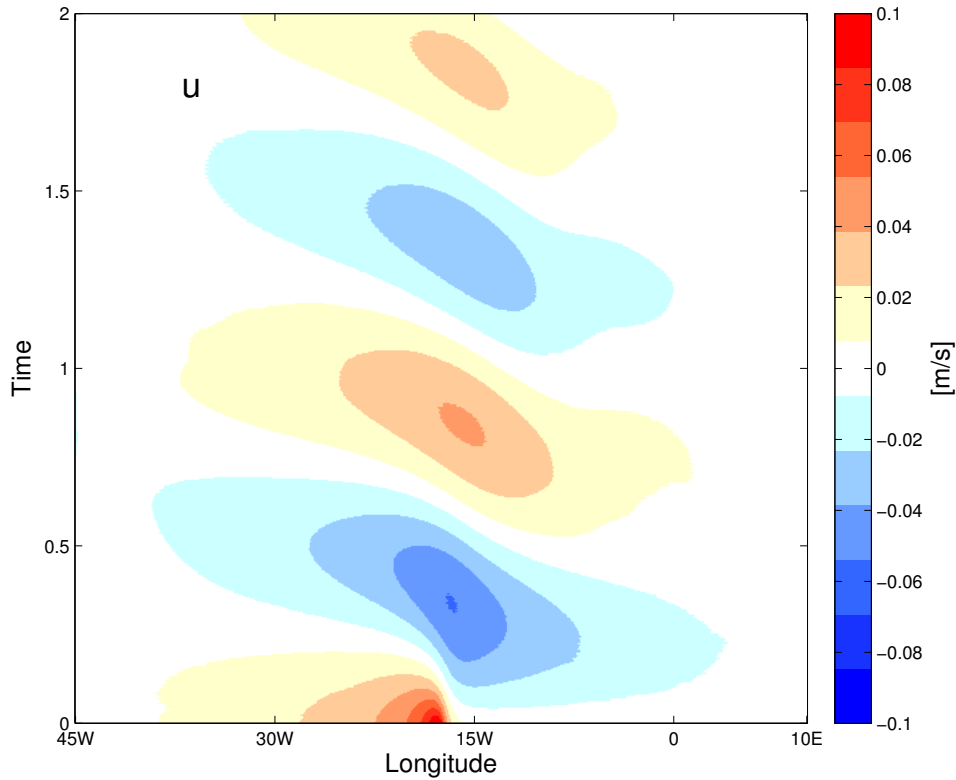


Figure. 3.1 | Time evolution of the zonal velocity for the gravest basin mode test case for $A_h = 10 \text{ m}^2/\text{s}$. Note that the time is normalized by the gravest equatorial basin mode period (1670 days), corresponding to $Time = 1$ in the figure. Units are noted along the colour bars.

Note that as a test experiment, a reduced gravity shallow water model is used. The governing equations are still the same as Eq. 12 - 14 but with the gravitational acceleration g replaced by reduced gravity g' , and the equivalent depth H_e by a water layer thickness H . In order to

keep the gravest basin mode period 1670 *days*, we choose the gravity wave speed $c = 0.17 \text{ m/s}$. A layer thickness $H = 200 \text{ m}$ is chosen for the consistency with the observed vertical scale of the equatorial deep jets; the reduced gravity g' is then equal to $1.445 \times 10^{-4} \text{ m/s}^2$. In this test model run, the lateral eddy viscosity A_h is set to be $10 \text{ m}^2/\text{s}$, and there is no external forcing applied to counter the dissipation. The other model parameters, such as the horizontal resolution, the integrating scheme, etc., are identical to the later model runs.

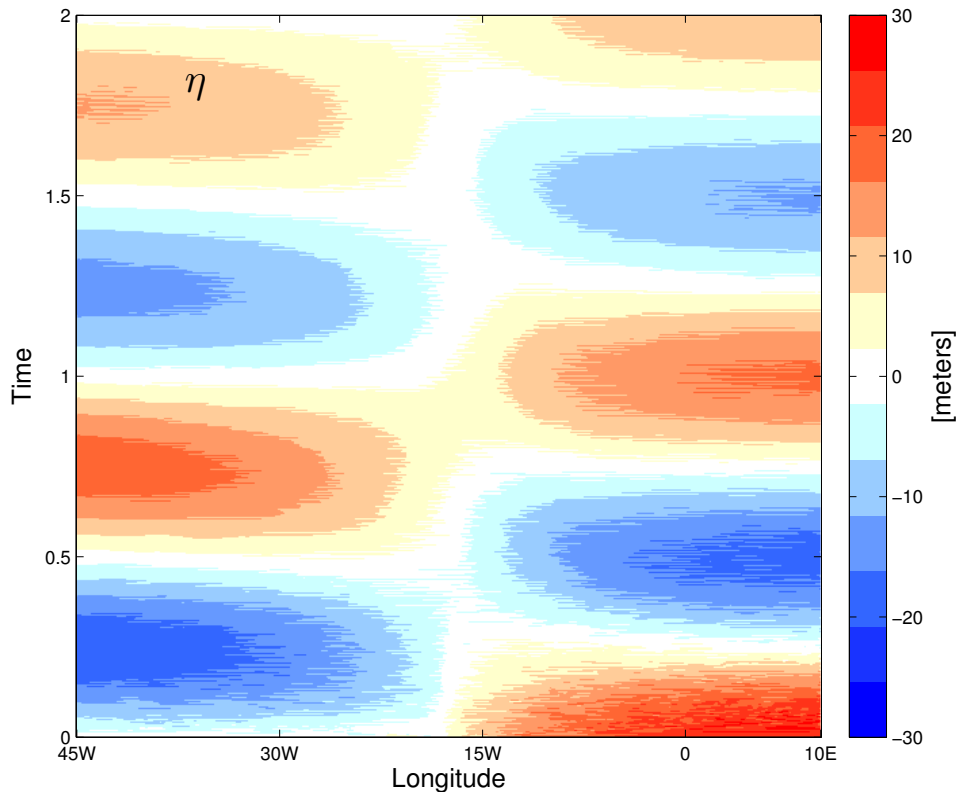


Figure. 3.2 | Time evolution of the interface displacement for the gravest basin mode test case for $A_h = 10 \text{ m}^2/\text{s}$. Note that the time is normalized by the gravest equatorial basin mode period (1670 *days*), corresponding to $Time = 1$ in the figure. Units are noted along the colour bars.

Fig. 3.1 and 3.2 illustrate the time evolution of both zonal velocity u and isopycnal displacement η along the equator within two oscillation periods. Similar to Fig. 3 in [Cane and Moore \(1981\)](#), both u and η alternate in sign with time, indicating the propagation of equatorially trapped Kelvin and long Rossby waves. However, the reducing amplitude of both variables with time reflects the dissipation caused by the lateral mixing. In the centre of the basin in Fig. 3.1, especially within the first oscillating cycle, a focusing caused by many different Rossby waves can be seen (see Fig. 3.12 discussed later).

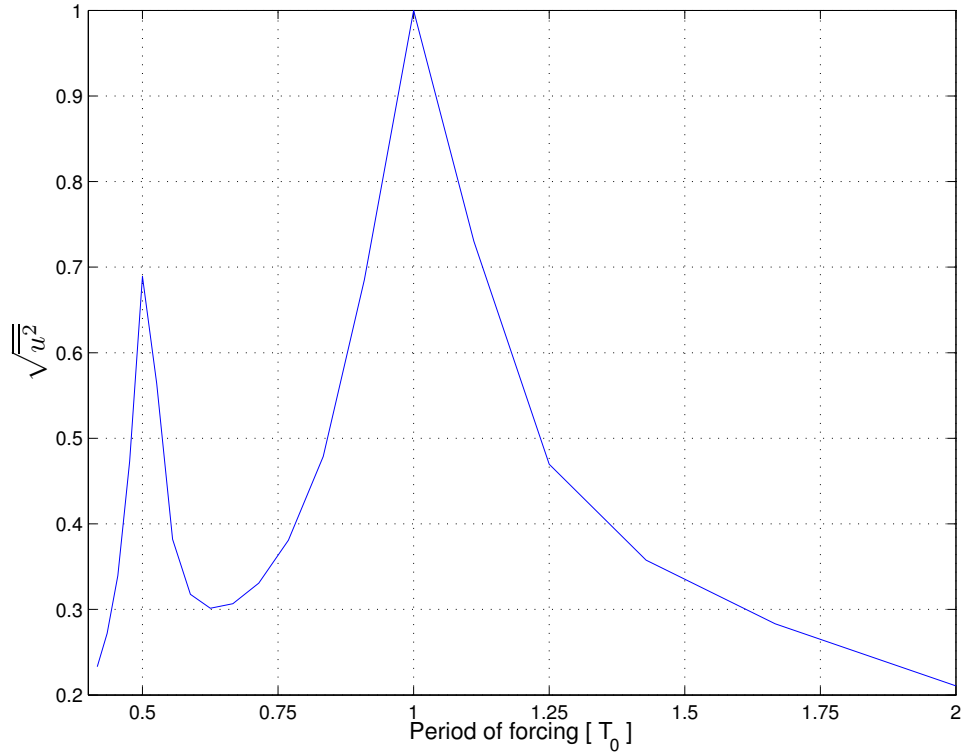


Figure. 3.3 | The square root of the zonally and temporally averaged square of the zonal velocity along the equator as a function of the period of the forcing. The time average is computed over the final steady oscillating cycle, and $A_h = 10 \text{ m}^2/\text{s}$. Note that along the x-axis, the period of forcing is normalized by the gravest basin mode period $T_B = 1670 \text{ days}$, and along the y-axis, the amplitude of $\sqrt{\overline{u^2}}$ is normalized by the maximum value.

After the test experiment of the gravest equatorial basin mode, we start to use the shallow water model for a high-order baroclinic vertical normal mode, given by Eq. 12 - 14. In order to overcome the dissipation shown in Fig. 3.1 and 3.2, a periodic zonal forcing (Eq. 20) is applied over the basin. To test for resonance with a basin mode, we started with a series of experiments forced by a spatially uniform forcing over the full basin given by Eq. 20, in which the oscillating period of the forcing (corresponding to $2\pi/\omega$) for each experiment differs from each other, but the amplitude of the forcing for each experiment stays constant, and $A_h = 10 \text{ m}^2/\text{s}$. We ran the model in each experiment until it comes to a steady oscillating state, which basically means that the input energy given by the forcing is equal to the dissipation caused by the lateral mixing, so the model output stays exactly the same from one cycle to the next. Then we recorded the last 10 complete oscillating cycles for each experiment corresponding to a given period of forcing.

Fig. 3.3 shows the square root of the zonally and temporally averaged square of the zonal

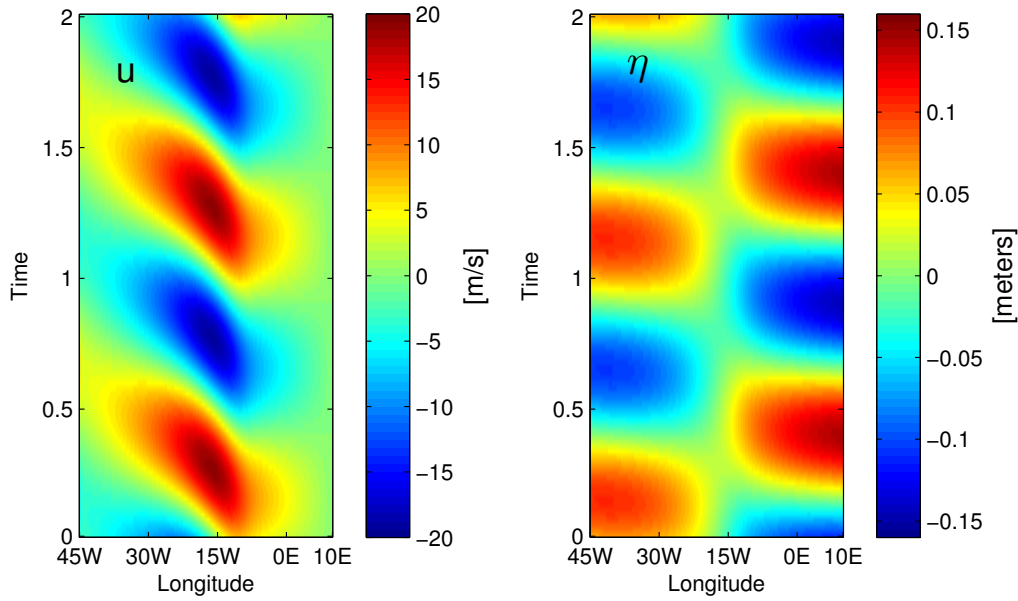


Figure. 3.4 | Time evolution of the zonal velocity (left) and the isopycnal displacement (right) along the equator for $A_h = 10 \text{ m}^2/\text{s}$ in the case “Full”. Positive u and η represent eastward velocity and downward isopycnal displacement, respectively. These two variables are plotted over the same time span in the steady oscillatory state. Note that due to the periodicity of the model output, only two complete oscillating cycles are shown here, and that the time is normalized by the model period (1670 days), corresponding to $Time = 1$ in the figure. Units are noted along the colour bars.

velocity along the equator as a function of the period of the forcing. The time average is calculated over the final steady oscillating cycle. It is clear that the largest response of the amplitude occurs when the period of wind forcing coincides the period of the gravest equatorial basin mode, which is 1670 days. Interestingly, a second peak occurs when the period of the forcing is half of the basin mode period, which corresponds to the second basin mode with twice the frequency of the gravest basin mode.

In order to keep the resonance and keep the model in a steady oscillating state after spin-up, all the following model runs without mean-flow, are set to have a fixed forcing amplitude, and fixed forcing period (1670 days). We first still keep the forcing spatially uniform over the full basin, and run the model with different values of A_h , in order to detect the effect of the lateral eddy viscosity term on the amplitude as well as the width of the equatorial deep jets. We set $A_h = 10, 50, 100, 200, 300, 400, 500, 600 \text{ m}^2/\text{s}$, respectively.

Fig. 3.4 shows the time evolution of the zonal velocity and the isopycnal displacement along the equator for the case of $A_h = 10 \text{ m}^2/\text{s}$. Exactly two cycles in the steady oscillating state are

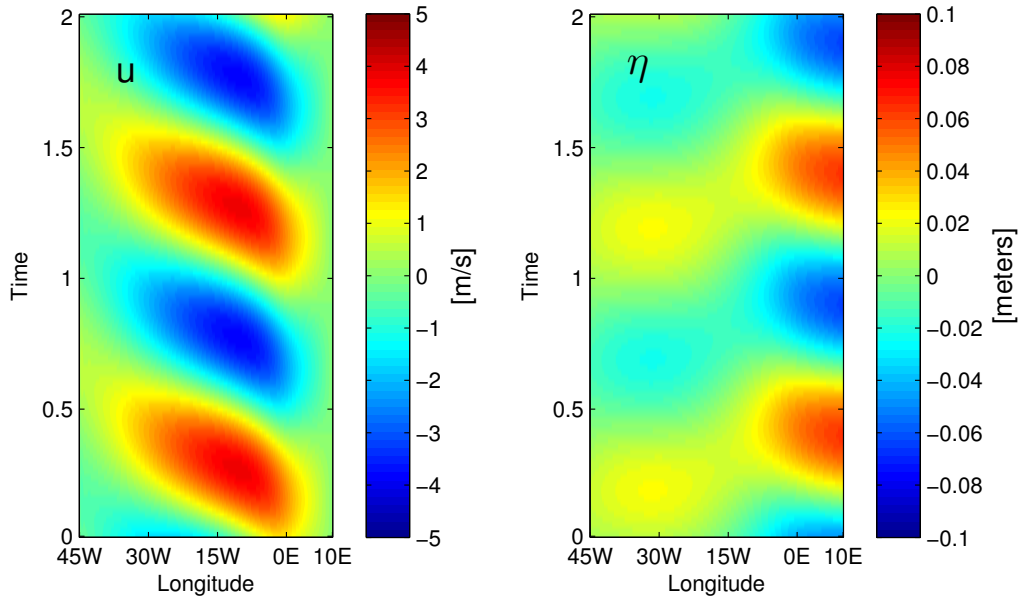


Figure. 3.5 | The same as in Fig. 3.4, except for $A_h = 200 \text{ cm}^2/\text{s}$. Exactly the same model time span of u and η is taken as in the $A_h = 10 \text{ m}^2/\text{s}$ case. Please notice that different scales are used for the colour bars for u and η compared to Fig. 3.4 and that the unit of each variable is the same as in Fig. 3.4.

shown, and the maximum amplitude of neither of the variables changes with time, so it can be concluded that the wind forcing (with a period of 1670 days) has successfully counteracted with the dissipation caused by the lateral mixing term.

Fig. 3.5 and Fig. 3.6 illustrate the same variables as in Fig. 3.4, except that $A_h = 200 \text{ m}^2/\text{s}$ and $A_h = 600 \text{ m}^2/\text{s}$, respectively. For all the cases, the time span over which u and η are plotted corresponds to the same model time range. Comparing the three lateral mixing cases, one can clearly see that the amplitudes of u and η strongly decrease as A_h increases, especially on the western side of the basin, indicating a strong damping effect of the lateral mixing term. Due to the smaller phase velocity of the equatorial Rossby waves (manifesting as a longer propagating time), the damping effect is greater on the Rossby waves than the Kelvin waves. A weak focusing can be sensed at the centre of the basin of the zonal velocity for $A_h = 10 \text{ m}^2/\text{s}$ (Fig. 3.4), while it does not appear in Fig. 3.5 or 3.6.

Before further proceeding, a few snapshots help us to have a direct impression of the model output as well as the effect of the lateral eddy viscosity term. Fig. 3.7a and 3.7b are snapshots of zonal velocity and isopycnal displacement for three different A_h cases taken simultaneously from the model. Zonally symmetric structure is obvious, and similar to the time evolution plots, the amplitude of the model response decreases as the lateral mixing coefficient increases.

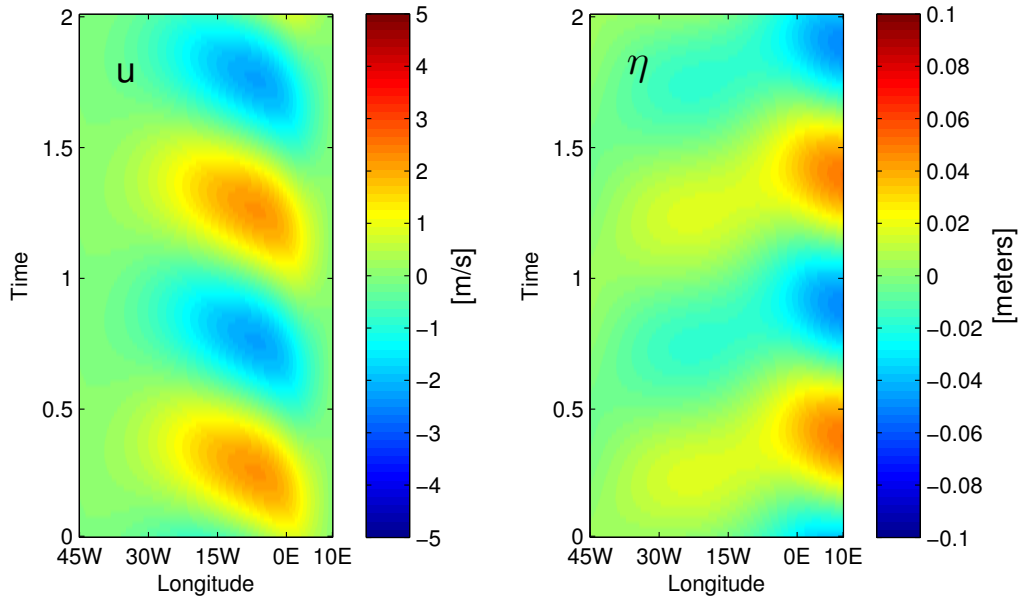


Figure. 3.6 | The same as in Fig. 3.4, except for $A_h = 600 \text{ cm}^2/\text{s}$. Exactly the same model time span of u and η is taken as in the $A_h = 10 \text{ m}^2/\text{s}$ case. Please notice that the scales for the colour bars are the same as in Fig. 3.5 and that the unit of each variable is the same as in Fig. 3.4.

On the eastern side of the basin, the zonal velocity has a maximum along the equator and decays on either side with latitude, — the signature of the equatorially-trapped Rossby waves.

In order to examine the influence of the lateral mixing of momentum on the horizontal structure of the Atlantic EDJs, we start with the forcing case “Full”. For each A_h in the “Full” case, the square root of the zonally and temporally averaged square of the zonal velocity, $\sqrt{u^2}$, is calculated, making it a function of latitude. The time average is computed over the final steady oscillating cycle, and the zonal average is done over the longitude range between 30°W and 15°W in the model domain. This longitude band is chosen in correspondence with the same longitude band used for processing the Argo float data (see Section 2.2). Fig. 3.8 shows this quantity for 8 different A_h values as a function of latitude between 2°S and 2°N . The results are zonally symmetric with maxima at the equator. It is obvious that the amplitude of $\sqrt{u^2}$ at the equator decreases dramatically as A_h increases.

We then normalize the quantity in Fig. 3.8 by the corresponding maximum value for each A_h case, so that the normalized results have the same dimensionless maximum as plotted in Fig. 3.9. It is clear that the curves become broader with increasing A_h . To measure the width L_e of the simulated EDJs quantitatively, we calculate the meridional distance over which $\sqrt{u^2}$ decreases to $1/e$ of its maximum value on the equator. This corresponds to, in Fig. 3.9, the

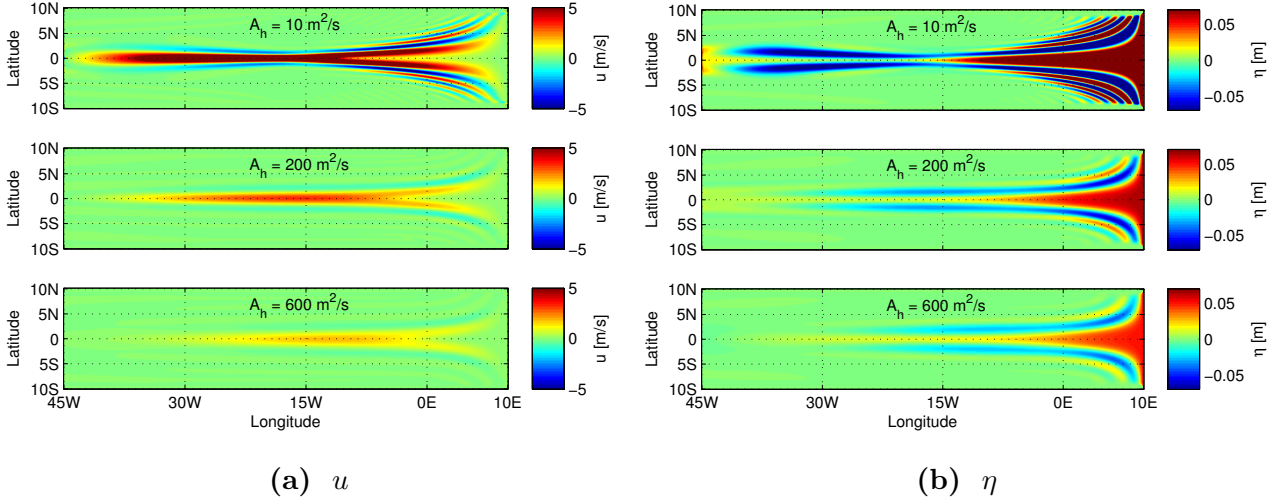


Figure. 3.7 | Simultaneous snapshots of zonal velocity (a) and isopycnal displacement (b) for the cases $A_h = 10, 200$ and $600 \text{ m}^2/\text{s}$, respectively. Please note that the colour bar scale for u or η is set to be identical in each case to simplify the comparison, and that all of these six snapshots are taken at the same time step in the model. The units are noted along the colour bars.

horizontal width of each curve at $\sqrt{u^2} = 1/e$ (black dashed line). The same process is then repeated to all the other forcing specifications, making a direct comparison between the effect of the different forcing locations possible.

Apart from all the model simulations, a theoretical prediction of the EDJ width as a function of A_h is given by a scale analysis, following [Greatbatch et al. \(2012\)](#). Under the approximation of an equatorial β -plane ([Gill, 1982](#)), we work in a limited range of latitudes centred around the equator. The unforced zonal momentum equation with the lateral mixing term is:

$$-A_h \nabla^2 u + \frac{\partial u}{\partial t} - \beta y v = -g \frac{\partial \eta}{\partial x} \quad (33)$$

where ∇ is the Laplacian operator given by

$$\nabla^2 = \frac{\partial^2}{\partial x^2} + \frac{\partial^2}{\partial y^2}$$

Its non-dimensional form is given by scaling the interface displacement η and time t with H and T , respectively; the horizontal length scale x and y with L and L_e , respectively, and zonal velocity u and meridional velocity v with U and V , respectively. We assume a basin, whose zonal length scale is considerably larger than the meridional length scale (i.e., $L_e \ll L$), and that zonal velocity decays exponentially as it moves away from the equator (i.e., $u = U e^{-y^2/L_e^2}$).

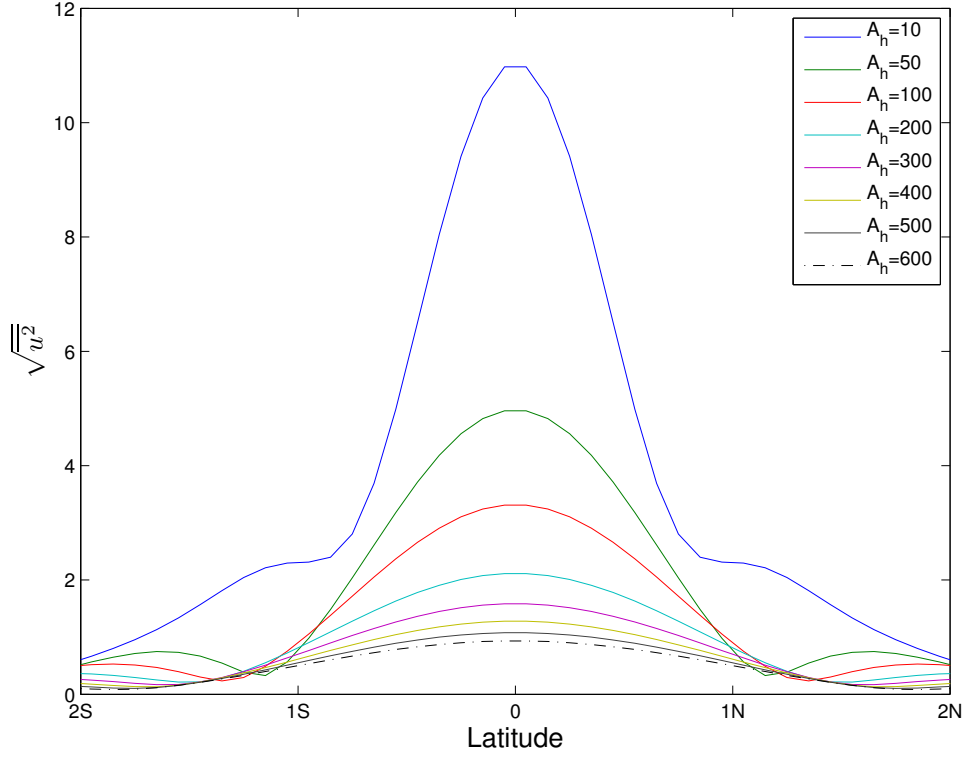


Figure. 3.8 | The square root of the zonally and temporally averaged square of the zonal velocity as a function of latitude, for the forcing case “Full” in the simulation without mean flow. All the A_h values used are shown here. The time average is computed over the final steady oscillating cycle, and the zonal average is done over the longitude range between $30^\circ W$ and $15^\circ W$ in the model domain. The unit of $\sqrt{u^2}$ is m/s, and the unit of A_h is m^2/s .

The balance of terms at the equator, $y = 0$, requires that

$$\left(\frac{2A_h}{L_e^2} + \frac{1}{T} \right) U = -g \frac{H}{L} \quad (34)$$

For $L_e \ll L$, the long wave approximation can be made, so the meridional momentum equation reduces to

$$\beta y u = -g \frac{\partial \eta}{\partial y} \quad (35)$$

Taking the y derivative of Eq. 35 and setting $y = 0$, it follows that

$$\beta u = -g \frac{\partial^2 \eta}{\partial y^2} \quad (36)$$

Assuming again that η has an e^{-y^2/L_e^2} dependence, the scaling shows that

$$\beta U = -g \frac{2H}{L_e^2} \quad (37)$$

Combining Eq. 34 and Eq. 37 gives a function of L_e :

$$L_e^4 - \frac{2L}{\beta T} L_e^2 - \frac{4A_h L T}{\beta T} = 0 \quad (38)$$

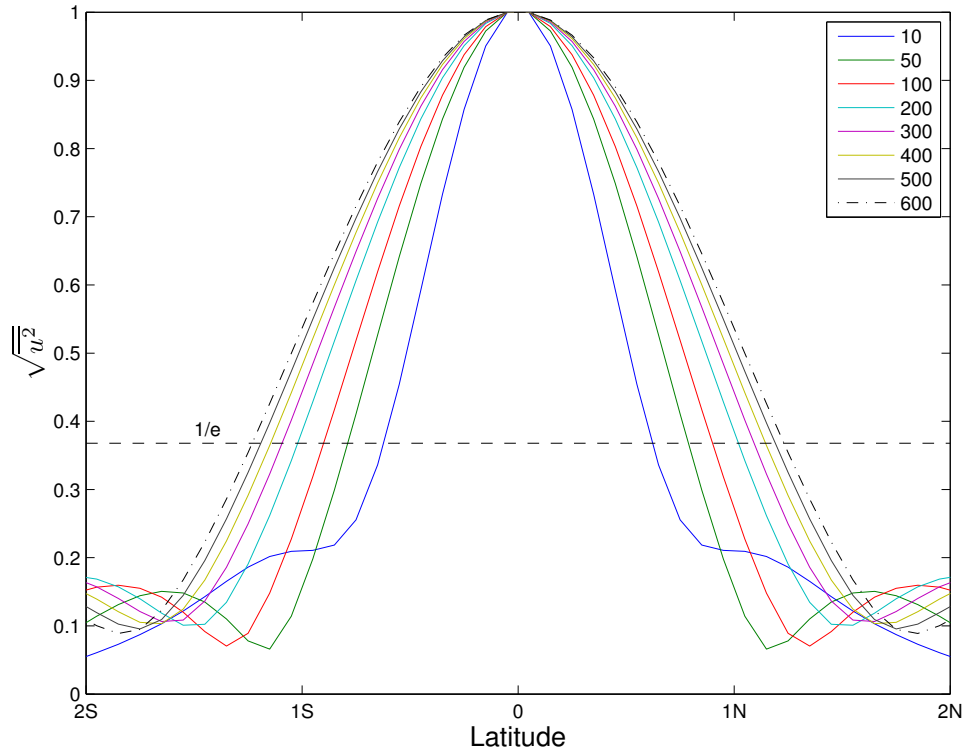


Figure. 3.9 | The same quantity as in Fig. 3.8, but normalized by the corresponding maximum for each case. Note that the units for A_h are the same as in Fig. 3.8.

Due to the dominance of the gravest Rossby wave in the model results for the “Full” case, we could argue that the phase velocity of $c/3$ ($c = \sqrt{gH}$) is approximately equivalent to the zonal width of the basin L divided by the time scale T as follows

$$\frac{c}{3} = \frac{L}{T}$$

Therefore, Eq. 38 becomes

$$L_e^4 - \frac{2c}{3\beta}L_e^2 - \frac{4A_hTc}{3\beta} = 0 \quad (39)$$

which can be solved as a quadratic equation with the result

$$L_e = \sqrt{\frac{c}{3\beta} + \sqrt{\frac{c^2}{9\beta^2} + \frac{4A_hTc}{3\beta}}} \quad (40)$$

As mentioned in the introduction, the meridional width of the observed Atlantic EDJs is found to be 1.5 times larger than the theoretical width implied by the vertical structure of the EDJs, based on linear inviscid theory (*Johnson and Zhang (2003)*). We can calculate the cross-equatorial width for the gravest Rossby wave in the same way as we calculated L_e for the model response, which gives a value of $L_e = 0.65^\circ$ for the model parameters. This value agrees

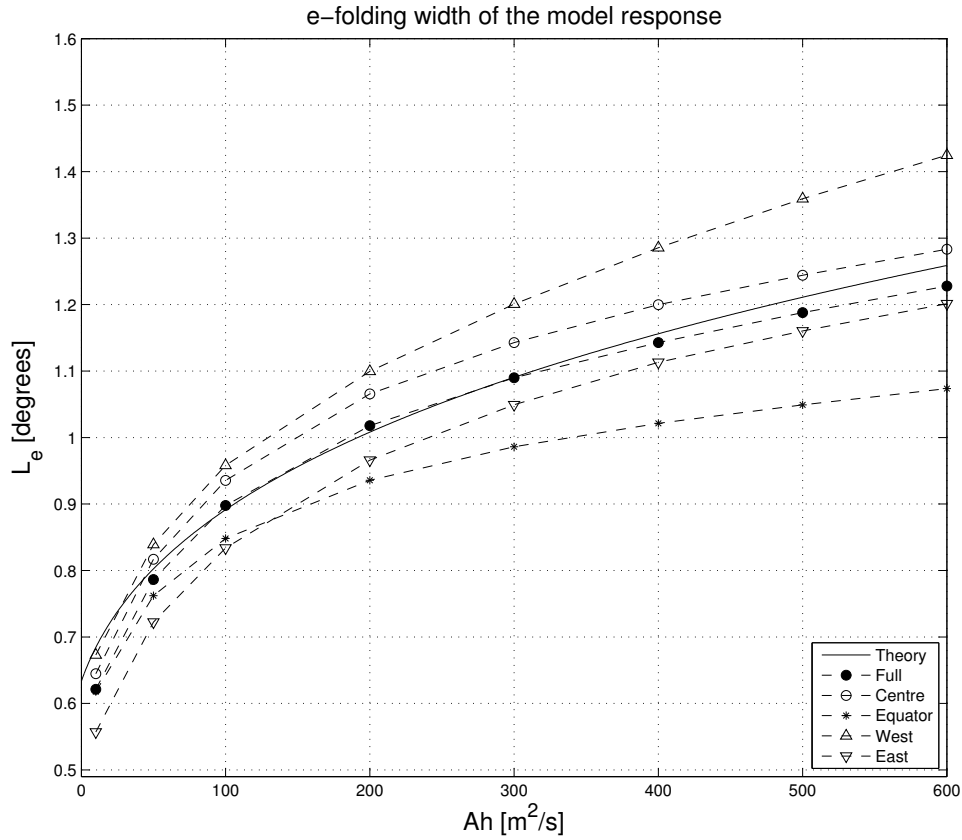


Figure. 3.10 | The e-folding width (in degrees latitude) of the model response for different values of the lateral mixing coefficient A_h . In the different cases, the forcing is applied over the whole basin (Full), the equatorial band (Equator), the west third of the basin (West), the centre third of the basin (Centre), and the east third of the basin (East). Please refer to subsection 2.1.1.3 for details of the forcing. The theoretical prediction of the width (Theory) is also plotted (Eq. 40).

with the theoretical width given by Eq. 40 at $A_h = 0$, as follows

$$L_e = \sqrt{\frac{2c}{3\beta}} \approx 0.63^\circ \quad (41)$$

To give a good fit to the model response (case “Full” in Fig. 3.10), T in Eq. 40 is chosen to be one third of the basin mode period ($1670/3 = 417.5$ days). The corresponding theoretical width is plotted as the black solid line in Fig. 3.10.

Fig. 3.10 shows the cross-equatorial width of the simulated EDJs as a function of A_h for different forcing specifications (cf. subsection 2.1.1.3 for details of the forcing). As expected, L_e increases as A_h increases in all the cases. The greatest width of the model response is given by the forcing “West”, the second is by the forcing “Centre”. Since the equatorial Kelvin wave has a greater cross-equatorial width than the gravest Rossby wave, this indicates a more important

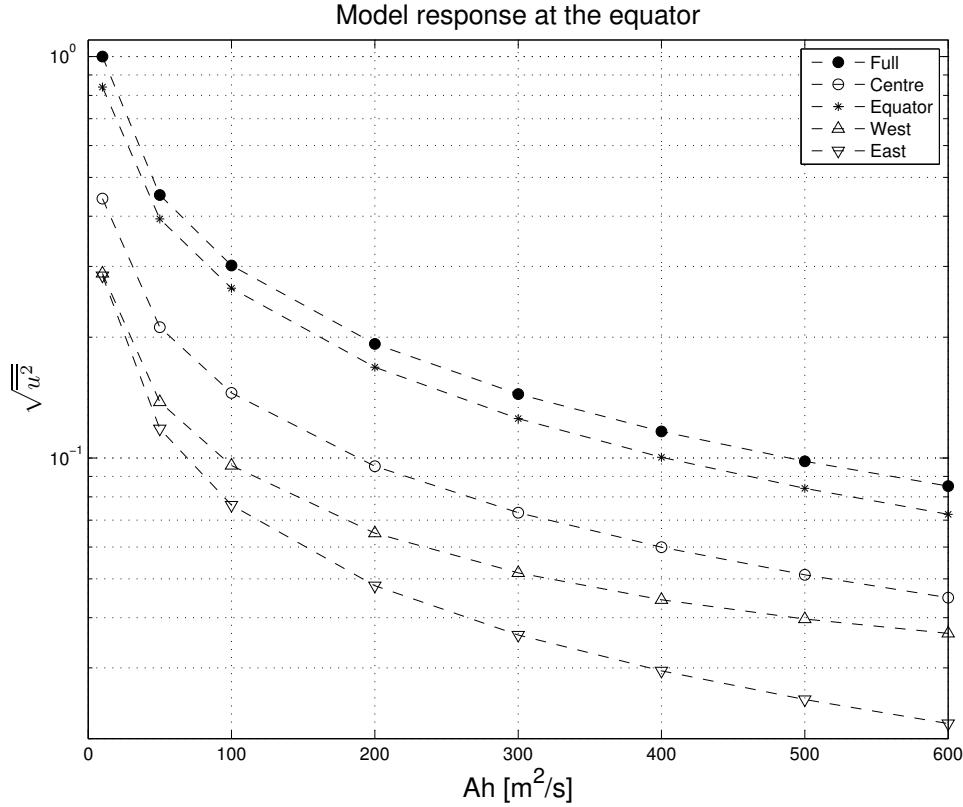


Figure. 3.11 | The square root of the zonally and temporally averaged square of the zonal velocity between 30°W and 15°W along the equator for different forcing specifications. Note that the label marks for the forcing are the same as in Fig. 3.10, and that this quantity is normalized by the largest value among all the forcing specifications. A logarithmic scale is used for the y-axis.

role of the Kelvin wave in these two cases in comparison with the cases “Full” and “East”, in which the gravest equatorial Rossby wave dominates (see Fig. 3.12 and 3.13 discussed later). A smaller width of the model response is given by the case “Equator”, and the dependence of the width on A_h in this case is also weaker than in the other cases, especially when A_h is larger than $200 \text{ m}^2/\text{s}$. However, if we take $1.5 \times 0.65^\circ = 0.98^\circ$ as a reference width of the observed Atlantic EDJs, the corresponding A_h value in our simulation case “Equator” is $300 \text{ m}^2/\text{s}$. This value is comparable with the value of $400 \text{ m}^2/\text{s}$ suggested by [Brandt et al. \(2008\)](#) to balance the reduction of oxygen concentration from west to east along the equator. Approaching $A_h = 0$ in Fig. 3.10, the widths of the simulated EDJs in different forcing cases also differ from each other. This is caused by the presence of many other Rossby waves that appear when the dissipation is too small to suppress them ([Greatbatch et al., 2012](#)).

In Fig. 3.11, the square root of the zonally and temporally averaged square of the zonal

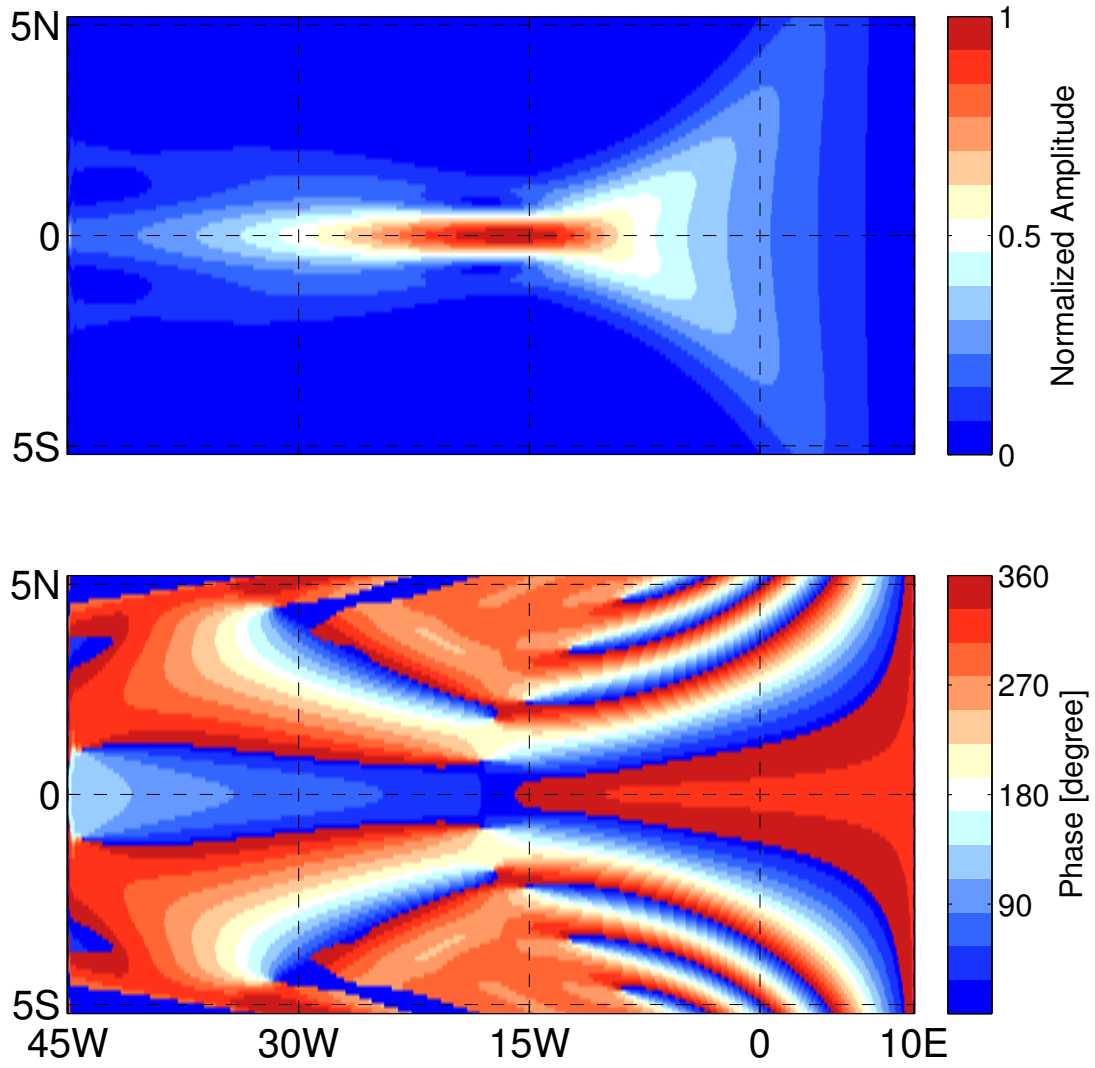


Figure. 3.12 | The amplitude and phase of the model zonal velocity for $A_h = 10 \text{ m}^2/\text{s}$ in the case “Full”. The amplitude is normalized by the maximum value of the model response. The phase is taken for one complete oscillating cycle, the zero-phase corresponding to the time point when the largest eastward zonal velocity along the equator occurs. A phase of 90 degrees means that at that location the maximum occurs by a lag of a quarter of the model period, compared to zero.

velocity along the equator for different forcing cases is plotted as a function of A_h . The zonal average is taken between 30°W and 15°W and the time average is taken over the final steady oscillating cycle. As we can see, in all the forcing specifications, the larger A_h is, the smaller the amplitude is. The largest model response on the equator results from the spatially uniform forcing (Full), and uniform forcing confined within the equatorial band (Equator) leads to the second largest model response. Among the other three cases, when the forcing is applied over the central third of the basin (centre), the model responds the largest, and the model amplitude

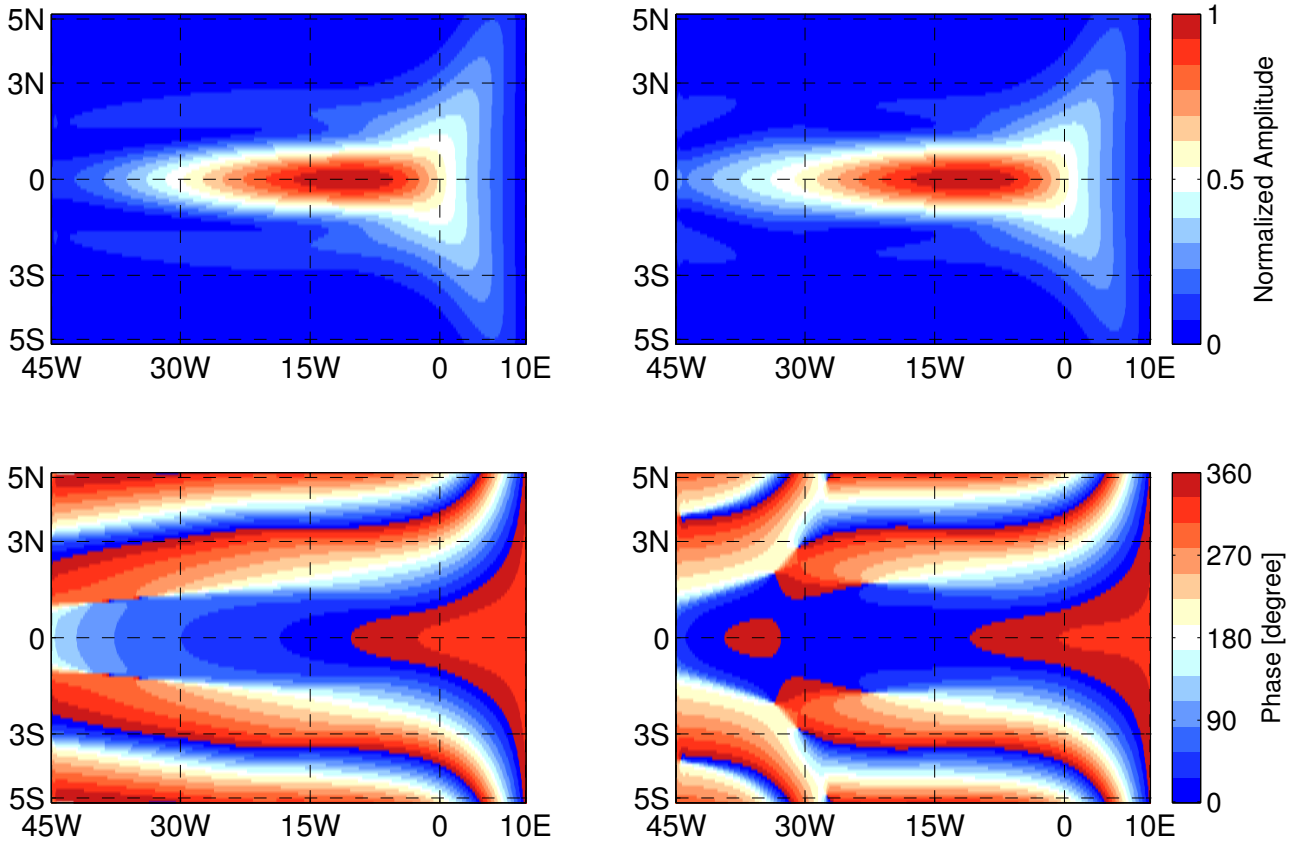


Figure. 3.13 | The amplitude and phase of the model zonal velocity for $A_h = 200 \text{ m}^2/\text{s}$ in the case “Full” (left) and “West” (right). The amplitude is normalized by the maximum amplitude in each plot. The phase is taken for one complete oscillating cycle, the zero-phase corresponds to the time point when the largest eastward zonal velocity along the equator occurs. A phase of 90 degrees means that at that location the maximum occurs by a lag of a quarter of the model period, compared to zero.

is smallest when the forcing is over the eastern third of the basin (East). Taking this result together, we may infer that the centre of the basin is the most efficient location to excite a equatorial basin mode, while the eastern third is the most inefficient location ([Greatbatch et al., 2012](#)).

To give a better understanding of the model response, the amplitude and phase of the zonal velocity for $A_h = 10 \text{ m}^2/\text{s}$ and $A_h = 200 \text{ m}^2/\text{s}$ in the case “Full” are shown in Fig. 3.12 and Fig. 3.13 (left), respectively. The amplitude of the model response is plotted as the maximum of the zonal velocity at each location in the model domain and is normalized by the largest value of the zonal velocity along the equator. The phase can be understood as the time step when the maximum eastward zonal velocity occurs at each grid point of the model domain, and the time step when the largest eastward zonal velocity along the equator occurs is marked

as the 0-phase. From this time on, one complete oscillating cycle of the model is taken into account, and the end point of this cycle is marked as 360°-phase.

It is not surprising that the maximum zonal velocity appears at the equator. A strong focusing at the centre of the basin can be seen for $A_h = 10 \text{ m}^2/\text{s}$. This feature appears in the analytic solution of [Cane and Moore \(1981\)](#) (cf. Fig. 1 and 2 in their paper) and is a consequence of the beta-dispersion of Rossby waves ([Schopf et al., 1981](#)). Looking at the phase plots for both A_h cases, we see a clear westward phase propagation, indicating the dominance of the gravest Rossby wave in the “Full” case. In the amplitude and phase for $A_h = 200 \text{ m}^2/\text{s}$ in the case “West” (Fig. 3.13 right), a eastward propagating signal can be observed on the western side of the basin, reflecting a more important role of the equatorial Kelvin wave in this forcing case.

3.1.2 Model Simulation with Background Mean Flow

In this simulation scenario, a barotropic mean flow (Fig. 2.1) is added to the shallow water equations (Eq. 22 - 24). We run the model under the influence of the mean flow with the same oscillatory forcing as before and examine the model response under different lateral mixing coefficients and different forcing locations, as we did in the simulation without mean flow.

Fig. 3.14 shows the square root of the zonally and temporally averaged square of the zonal velocity along the equator as a function of the period of the forcing. It is produced in the same way as used for Fig. 3.3. Though the plot still shows two principal peaks, the peaks are not located exactly at period 1 and period 0.5 of the forcing as in the simulation without mean flow. This shift implies that the largest model response tends to occur at a shorter period of the forcing, which is due to the “Quasi-Doppler shift” resulting from the mean flow ([Gerkema et al., 2013](#)). However, since period 1 of the forcing locates within the range of the resonance peak, and in order to compare with the former simulations, we still keep the period of the forcing identical to the period of the gravest equatorial basin mode (1670 *days*), and keep the amplitude of the forcing the same as used in the simulation without mean flow.

Looking at the time evolution of u and η for $A_h = 10 \text{ m}^2/\text{s}$ in the “Full” case (Fig. 3.15), we see that the model response to the wind is in a steady oscillating state. Different from the same case in the simulation without mean flow (Fig. 3.4), no focusing can be sensed at the centre of the basin in the u plot, while in the η plot, the damping on the western side of the basin relative to the eastern side is stronger. This implies a more dominant role of the gravest equatorial Rossby wave in this case. The time evolution for $A_h = 200$ and $600 \text{ m}^2/\text{s}$ (Fig. 3.16

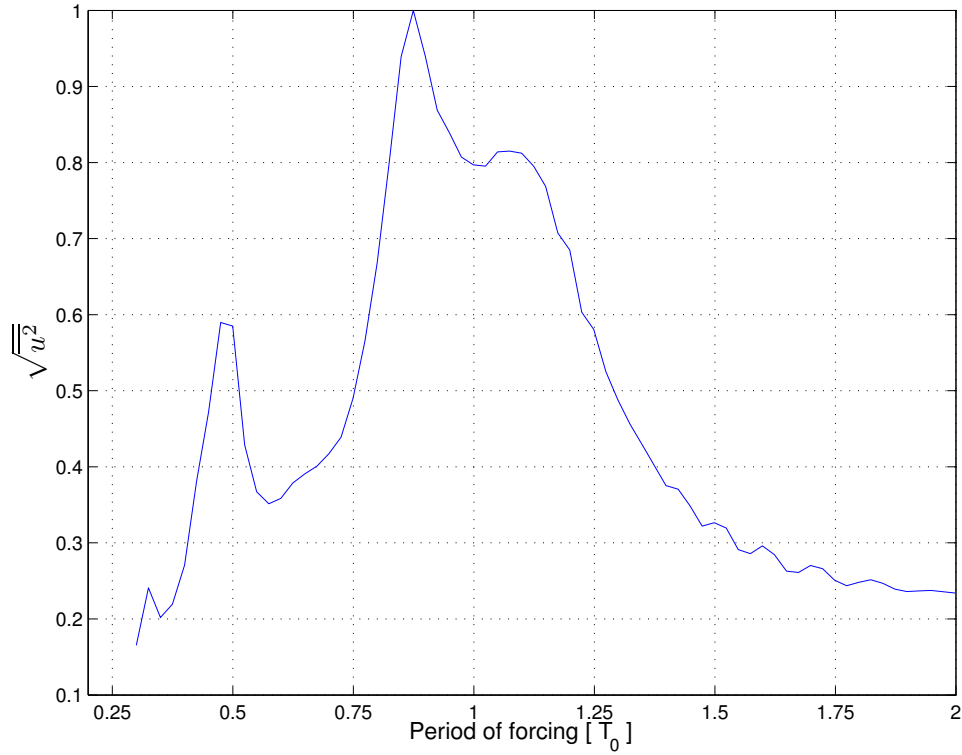


Figure. 3.14 | The square root of the zonally and temporally averaged square of the zonal velocity along the equator as a function of the period of the forcing. The time average is calculated over the final steady oscillating cycle, the zonal average is taken across the whole basin, and $A_h = 10 \text{ m}^2/\text{s}$. Note that along the x-axis, the period of the forcing is normalized by the gravest basin mode period $T_B = 1670 \text{ days}$, and that along the y-axis, the amplitude of $\sqrt{\overline{u^2}}$ is normalized by the maximum value.

and 3.17) shows a similar result as in the same A_h case in the simulation without mean flow (Fig. 3.5 and 3.6, respectively): the amplitude of the model response decreases as A_h increases, and on the western side of the basin, the quantities are damped stronger than on the eastern side.

Snapshots of u and η are taken at the same time step in the model for different A_h values. They also show a very clear decrease of the amplitude of the model response as A_h increases. However, a rather complicated structure reflects the influence of the background mean flow. Though it is not zonally symmetric, a Rossby-wave-like structure still can be seen on the eastern side of the basin, with the maximum zonal velocity along the equator, and decaying away from the equator with latitude. For $A_h = 10 \text{ m}^2/\text{s}$, η alternates in sign along about 5°S , similar feature exists at the same latitude close to the eastern boundary of the basin in η plots for $A_h = 200$ and $600 \text{ m}^2/\text{s}$. This feature will be discussed later (see Fig. 3.21).

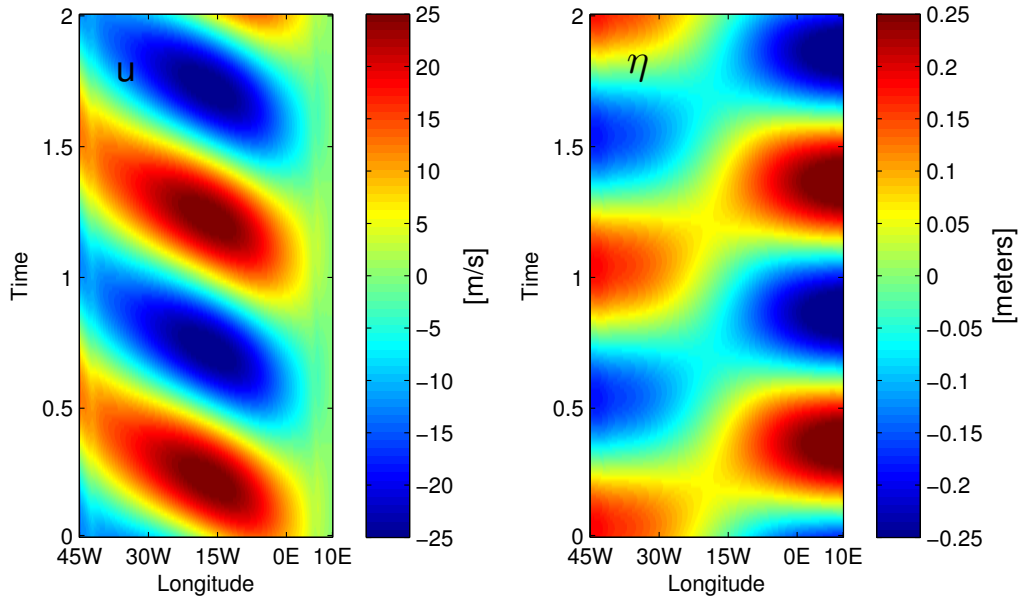


Figure. 3.15 | Time evolution of the zonal velocity (left) and the isopycnal displacement (right) along the equator for $A_h = 10 \text{ m}^2/\text{s}$ in the case “Full” in the simulation with mean flow. Positive u and η represent eastward velocity and downward isopycnal displacement, respectively. These two variables are plotted over the same time span in the steady oscillatory state. Note that due to the periodicity of the model output, only two complete oscillating cycles are shown here, and that the time is normalized by the model period (1670 days), corresponding to $Time = 1$ in the figure. The units are noted along the colour bars.

We follow the same procedure to calculate the cross-equatorial width of the model response in this simulation scenario as we used for the simulation without mean flow. The square root of the zonally and temporally averaged square of the zonal velocity between $30^\circ W$ and $15^\circ W$ for each specification of A_h and forcing is first calculated, then it is normalized by the corresponding maximum value in each case; finally, we use the meridional width at which this quantity decreases to $1/e$ of its maximum value at the equator to measure the cross-equatorial width of the simulated EDJs. The e-folding width of the model response as a function of A_h for different forcing cases in the simulation with mean flow is shown in Fig. 3.19. In comparison with the simulation without mean flow (Fig. 3.10), the width for all the A_h values in the case “West” exceeds that in the same forcing case of the former scenario by at least 0.5 degrees. This mirrors a greater impact of the equatorial Kelvin wave on the width in the presence of the background mean flow than without mean flow. In the case “East”, the width tends to be smaller by about 0.5 degrees, when A_h is greater than $200 \text{ m}^2/\text{s}$. The width in the case “Full” is slightly larger and the width in the cases “Centre” and “Equator” have little change.

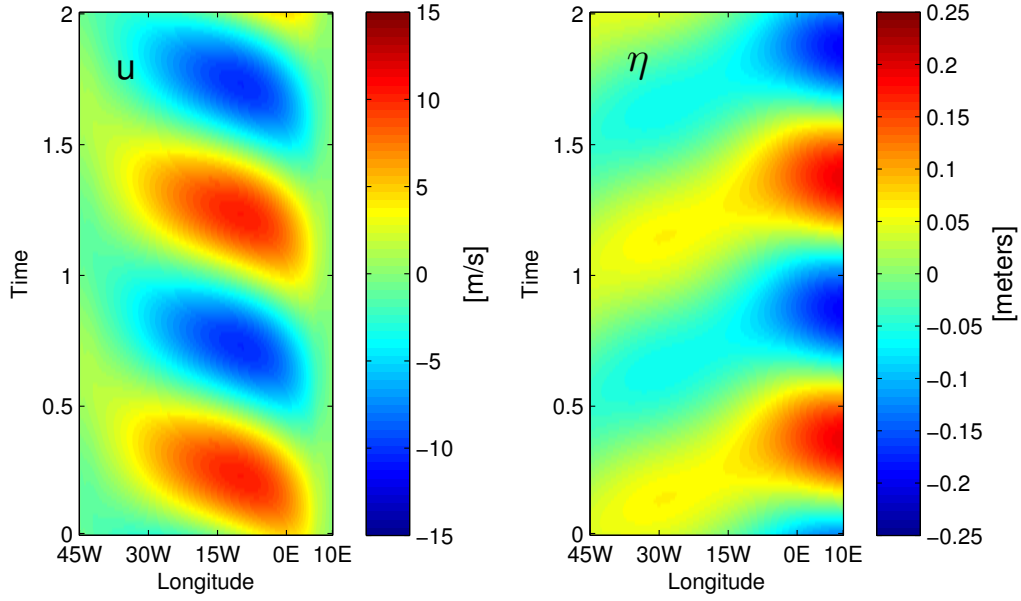


Figure. 3.16 | The same as in Fig. 3.15, except for $A_h = 200 \text{ cm}^2/\text{s}$. Exactly the same model time span of u and η is taken as in the $A_h = 10 \text{ m}^2/\text{s}$ case. Please notice that different scales are used for the colour bars for u and η compared to Fig. 3.15. The units are noted along the colour bars.

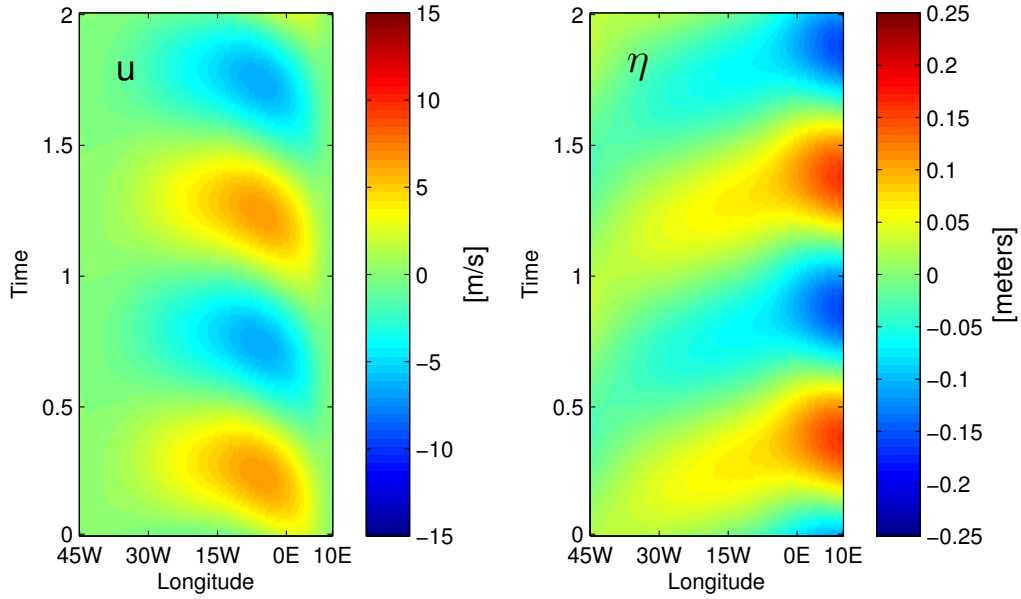


Figure. 3.17 | The same as in Fig. 3.15, except for $A_h = 600 \text{ cm}^2/\text{s}$. Exactly the same model time span of u and η is taken as in the $A_h = 10 \text{ m}^2/\text{s}$ case. Please notice that the scales for the colour bars are the same as in Fig. 3.16. The units are noted along the colour bars.

Comparing the width in the case “Full” with the theoretical prediction (the same as in Fig. 3.10), we see that they are not largely removed from each other (the case “Full” indicating

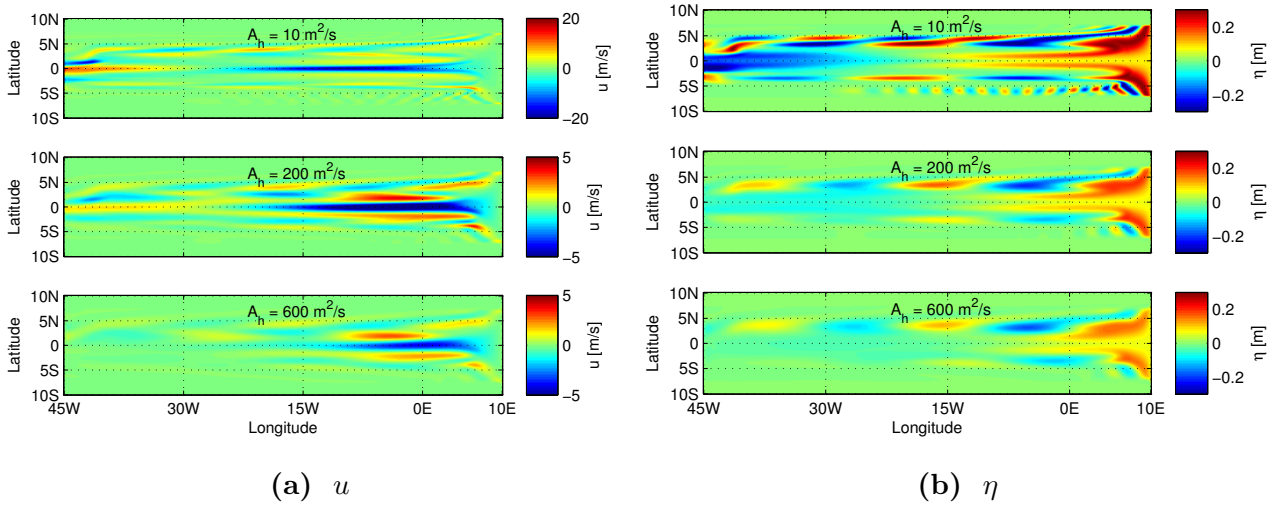


Figure. 3.18 | Simultaneous snapshots of zonal velocity (a) and isopycnal displacement (b) for $A_h = 10$, 200 and $600 \text{ m}^2/\text{s}$ in the “Full” case with mean flow, respectively. Please note that the colour bar scale for u is different for $A_h = 10 \text{ m}^2/\text{s}$ and that for η it is set to be identical in each case to simplify the comparison, and that all of the six snapshots are taken at the same time step in the model. The units are noted along the colour bars.

slightly larger width), and in general the curve “Theory” is still a reasonable estimate to the model response of the “Full” case in the simulation with mean flow.

The square root of the zonally and temporally averaged square of the zonal velocity along the equator as a function of the lateral mixing coefficient A_h for the simulation with mean flow is shown in Fig. 3.20. Following the same process as before, the square of the zonal velocity is averaged zonally between 30°W and 15°W , and temporally over the final steady oscillating cycle. As we see, for all the forcing cases, the model response is overall greater than that in the simulation without mean flow. However, as A_h increases, the amplitude of the model response decreases as before. $\sqrt{u^2}$ is still largest in the forcing case “Full”, followed by “Equator”, “Centre” and “West”, and is smallest in the case “East”. Therefore, the conclusion about the efficiency of the forcing location, i.e. the centre of the basin, made in the former section is still valid here.

The amplitude and phase for $A_h = 10$ and $200 \text{ m}^2/\text{s}$ in the forcing case “Full” (Fig. 3.21) are produced by the same method as used before. It shows a rather complicated structure for both A_h cases, especially off the equator. For example at about 4°N , there are bands with enhanced amplitude of the zonal velocity; these are the off-equatorial wave guides induced from the mean flow. There are also bands in which the zonal velocity remains nearly zero through the whole

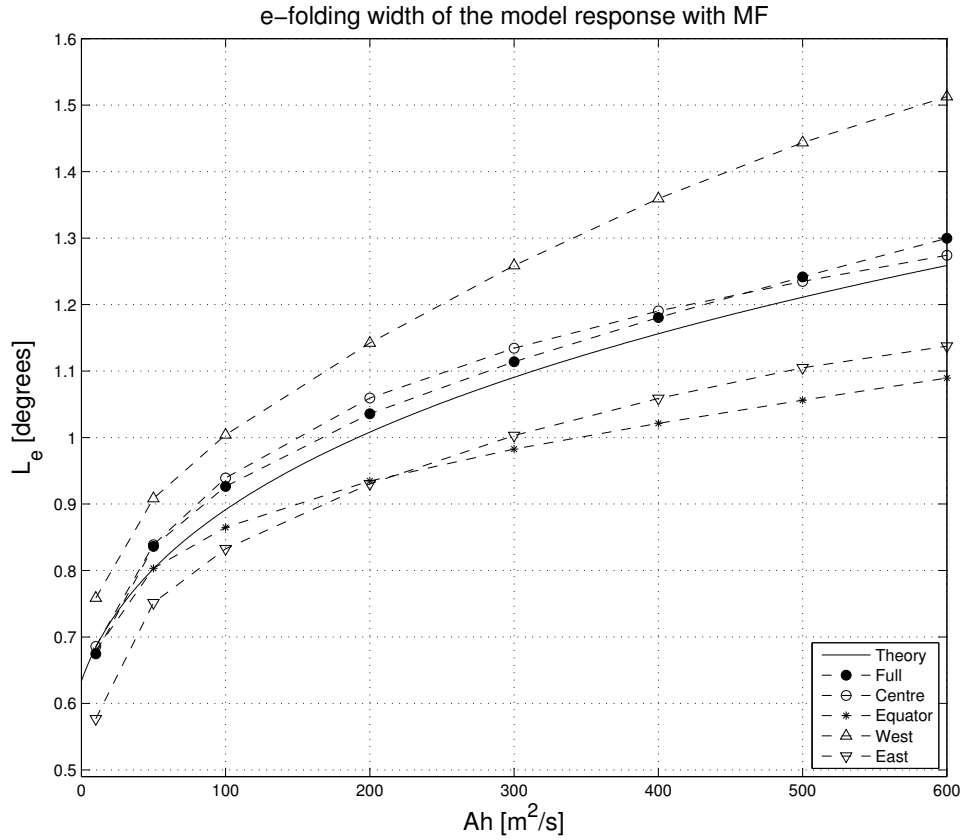


Figure. 3.19 | The e-folding width (in degrees latitude) of the model response in the simulation with mean flow for different values of the lateral mixing coefficient A_h . In the different cases, the forcing is applied over the whole basin (Full), the equatorial band (Equator), the west third of the basin (West), the centre third of the basin (Centre), and the east third of the basin (East). Please refer to Section 2.1.1.3 for details of the forcing. The theoretical prediction of the width (Theory) for the case without mean flow is also plotted (Eq. 40).

oscillating cycle, for example at about $3.5^\circ S$ for $A_h = 10 \text{ m}^2/s$, the corresponding phase shows a discontinuity at the same latitude as well. This may result from the strong zonal velocity of the mean flow that would damp and absorb the energy of the waves, preventing the wave penetration. The phase also shows a dominant westward propagation along the equator, and the Rossby wave structure near the eastern boundary of the basin, indicating the dominance of the gravest equatorial Rossby wave. However, compared with the simulation without mean flow, the Rossby wave focusing at the centre of the basin vanishes even for the small A_h value of $10 \text{ m}^2/s$. Note that at about $5^\circ S$ in the phase for $A_h = 10 \text{ m}^2/s$, we see the similar alternating structure as shown in Fig. 3.18, this could be considered as the extension of the Rossby wave fronts that are tilted into the zonal direction in the presence of the mean flow. This may also reflect some instability induced from the mean flow, although the amplitude of the zonal

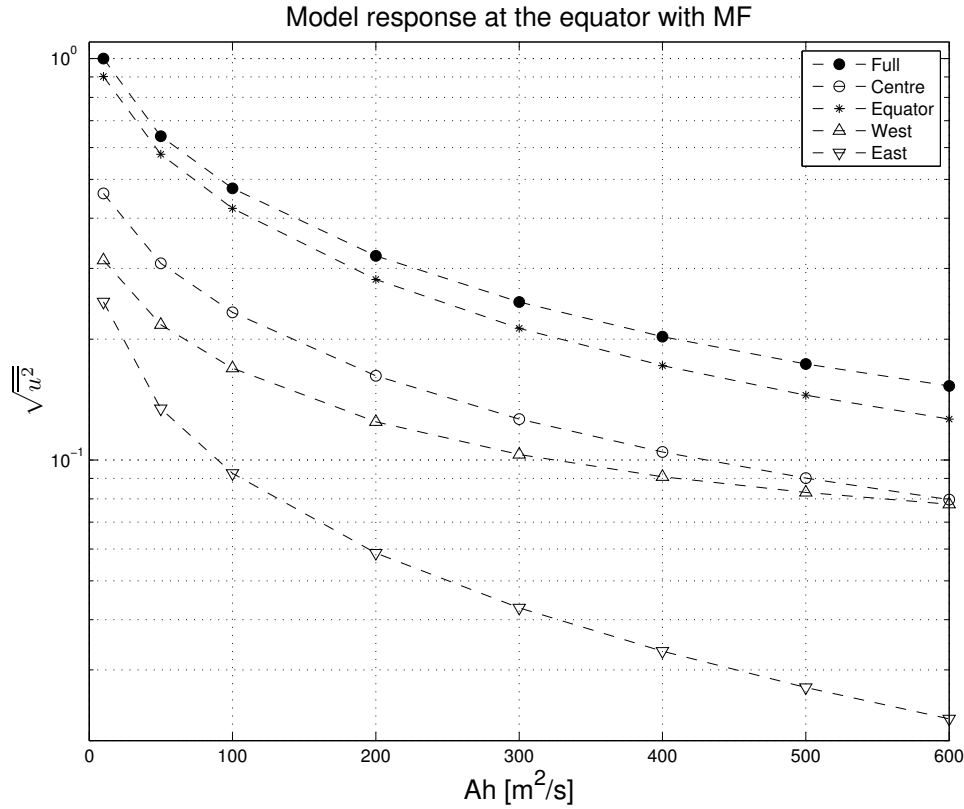


Figure. 3.20 | The square root of the zonally and temporally averaged square of the zonal velocity between $30^\circ W$ and $15^\circ W$ along the equator for different forcing cases in the simulation with mean flow. Note that the label marks for the forcing are the same as in Fig. 3.19, and that this quantity is normalized by the largest value among all the forcing specifications. A logarithmic scale is used for the Y-axis.

velocity at this location is very small compared to that at the equator. Also, these features do not grow with time in the model runs, and oscillate in the same period as the gravest basin mode, and they decrease in the model runs with high values of A_h . Therefore, we still consider them to be physically reasonable. Moreover, the structure of the phase for both A_h are very similar, indicating a very weak dependence of the phase on A_h .

3.2 Comparison with Observation

3.2.1 Profile Comparison

As mentioned above, to quantitatively compare our modelled Atlantic EDJs with observation, we use the Argo float data with parking depth of around 1000 meters between $30^\circ W$ and $15^\circ W$. The missing values and the velocities with an error estimate greater than 2 cm/s , as well as the

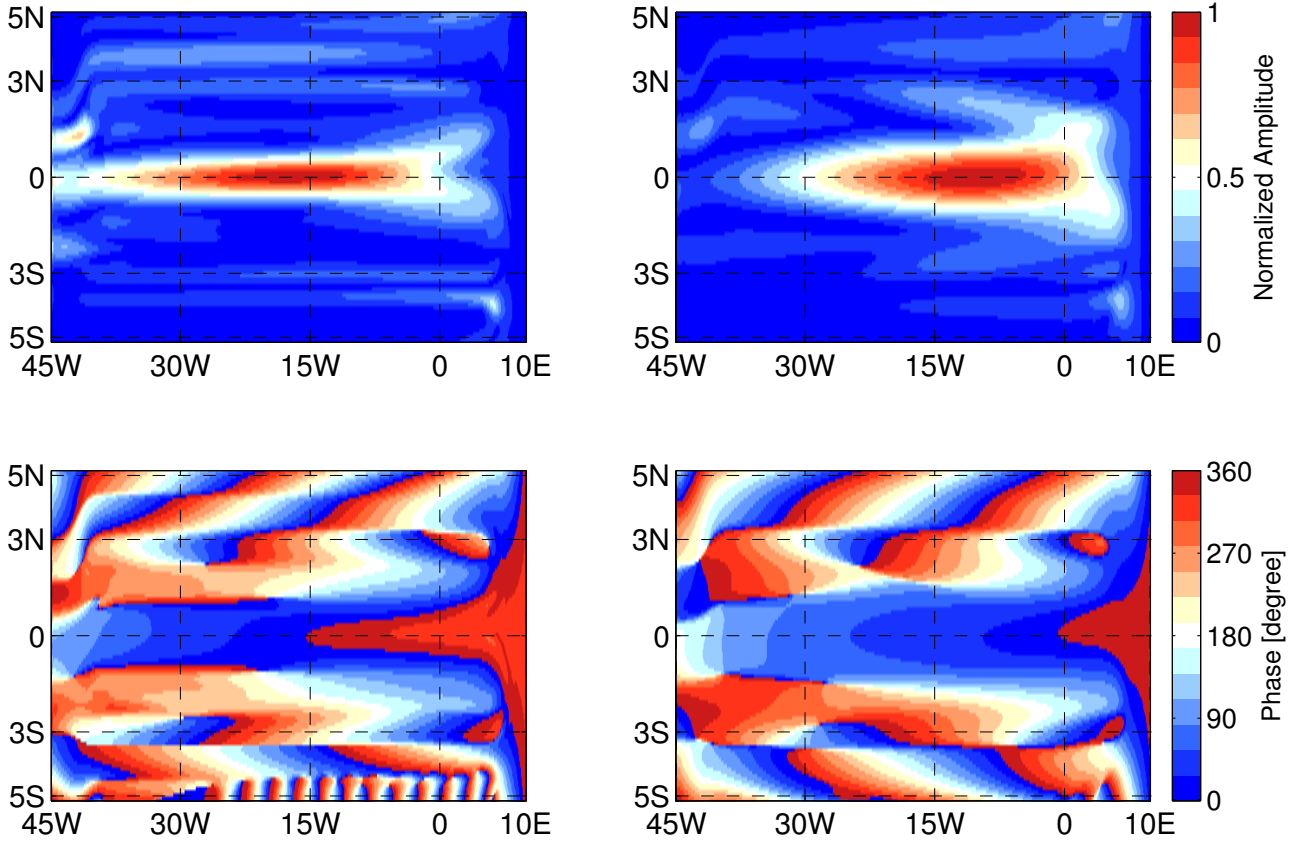


Figure. 3.21 | The amplitude and phase of the model zonal velocity for $A_h = 10 \text{ m}^2/\text{s}$ (left) and $A_h = 200 \text{ m}^2/\text{s}$ (right) in the case “Full” in the simulation with mean flow. The amplitude is normalized by the maximum amplitude in each plot. The phase is taken in one complete oscillating cycle, the zero-phase corresponds to the time point when the largest eastward zonal velocity along the equator occurs. A phase of 90 degrees means that at that location the maximum occurs by a lag of a quarter of the model period, compared to zero.

velocities greater than 4 times of the standard deviation from the mean of the zonal velocity at 1000 dbar depth are excluded to remove the outliers. We choose this longitude band based on the availability of the Argo float data through the entire recording time (Fig. 2.3).

After outliers are removed, the Argo float data are first binned into overlapping latitude bands of 0.5° width, the distance between the centres of every two closest bins is 0.2° . Then the data in each bin are sorted in the order of the time of the measurement, regardless of the longitude. Finally, a 1670-day harmonic is fitted to the sorted time series in each bin, resulting in a meridional profile of the amplitude of the harmonic fit with a resolution of 0.2° latitude. The harmonic fit to the equatorial bin (centred at 0° latitude) is demonstrated in Fig. 3.22. The blue dots are zonal velocities from the Argo float data, the green curve is the corresponding harmonic fit. As we see, the 1670-day harmonic fit represents the structure of

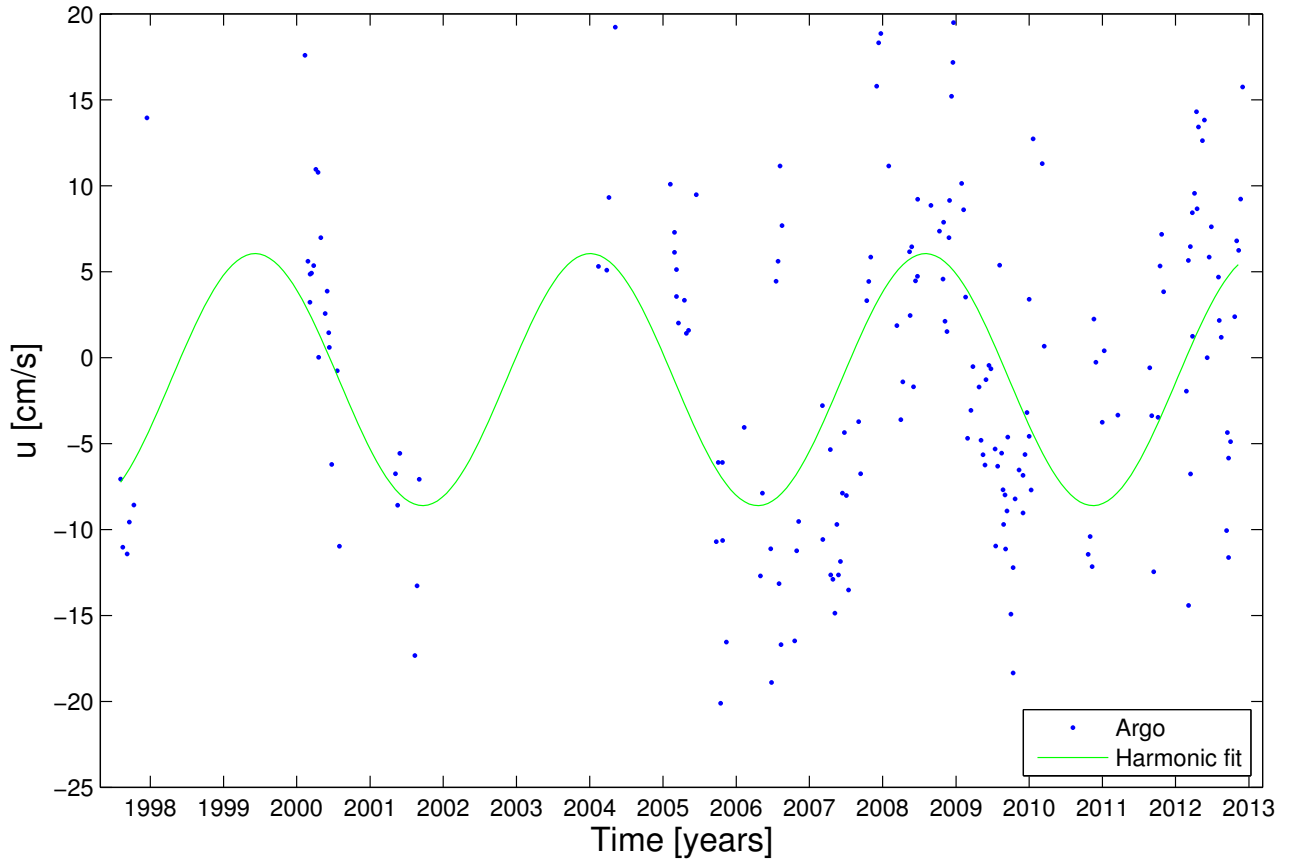


Figure. 3.22 | The 1670-day harmonic fit for the equatorial bin (centred at 0° latitude). The dots are the sorted zonal velocity from the Argo float data in cm/s, the green curve is the corresponding harmonic fit.

the Argo float data very well and it explains about 27% of the variance of the observed data. Here one assumption must be made: all the zonal velocities laying between $30^\circ W$ and $15^\circ W$ are in the same phase².

Fig. 3.23 is a update version of Fig. 5 in *Greatbatch et al. (2012)*. It shows the square of the amplitude of the 1670-day harmonic fit to the zonal velocity from the Argo float data as a function of latitude. The data we used were measured from August 1997 to May 2013, this duration of measurement is about 1.5 years (almost one third of the gravest equatorial basin mode period) longer than that used in *Greatbatch et al. (2012)*. Comparing with their result, though the zonal velocity shares a similar structure with a strong bias towards the northern side of the equator, the overall amplitude of the zonal velocity is smaller. This could be attributed to the increased available measurements in the updated version of the Argo float data, which

²Certainly, they are not in exactly the same phase, however, 15° longitude accounts for less than 7% of the zonal wavelength given by the gravest basin mode period $T = 1670$ days and the gravity wave speed $c = 0.17$ m/s.

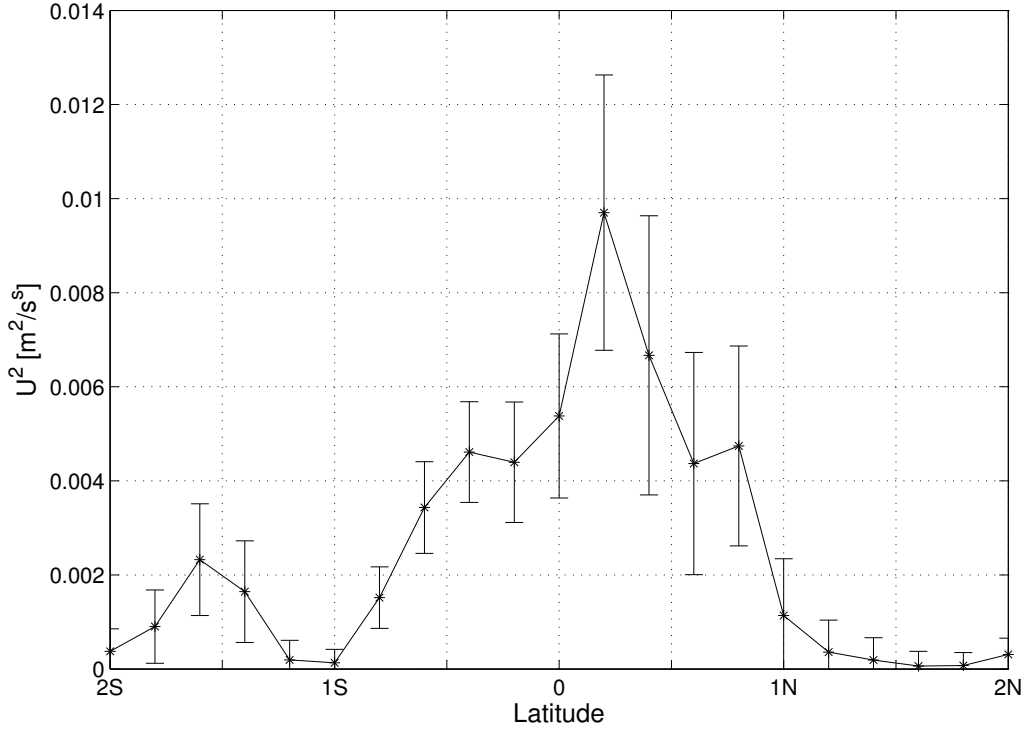


Figure. 3.23 | The square of the amplitude of the 1670-day harmonic fit to the zonal velocity from the Argo float data as a function of latitude. The Argo float data used here are measured between $30^\circ W$ and $15^\circ W$ with the parking depth of about 1000 m. The measurement period is August 1997 to May 2013. The error bars are calculated assuming each measurement to be independent.

decreases the dependence of the fitted amplitude on the exceptional large values that can be seen in Fig. 3.22 between the years 2006 and 2009. The error bars show the estimated error of the harmonic fit given by Eq. 43 with the assumption that all the measurements are independent, despite the fact that in reality there is some autocorrelation, which would increase the error bars.

Following [Brandt et al. \(2011\)](#), the harmonic analysis of the zonal velocity is performed by fitting a linear regression model in a least-squares sense to the Argo data as follows,

$$d_m = GA = A_1 I_N + A_2 \cos(\omega t) + A_3 \sin(\omega t) \quad (42)$$

where d_m is the fitted data vector of length N , t is the time vector of the data of the same length; G is the regression model matrix in the size of $N \times 3$, consisting of 1, $\cos(\omega t)$ and $\sin(\omega t)$ in either of the three columns, respectively, and each of the columns has the same element in the length of N ; $\omega = 2\pi/T_B$ is the angular frequency and $T_B = 1670$ days is the gravest basin model period, and A is a column vector of the regression factors (A_1 , A_2 and A_3). The error

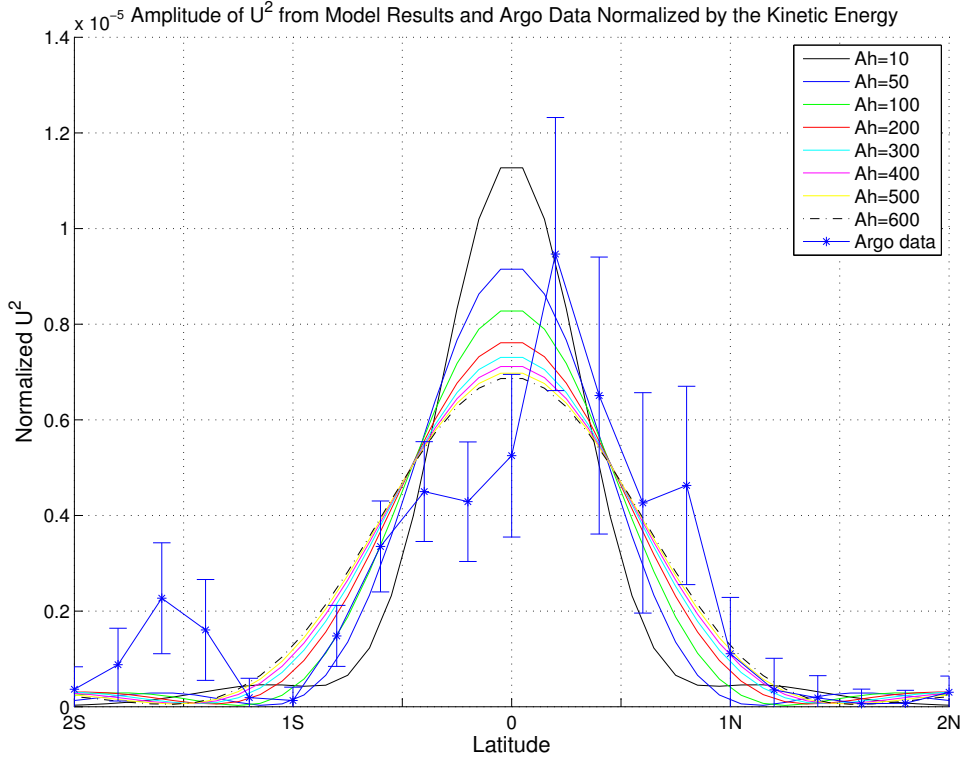


Figure. 3.24 | A comparison between the cross-equatorial profiles of the square of the zonal velocity $\overline{u^2}$ from the model simulation for the case “Equator” in the simulation without mean flow and the Argo float data. Note that the zonal velocities squared from both model and Argo float data, together with the error bars, are normalized to give the same area under each curve between $1^\circ S$ and $1^\circ N$. The unit of A_h is m^2/s .

matrix is given by

$$\Delta A = \sqrt{\frac{(G^T G)^{-1}[(d - d_m)^T (d - d_m)]}{n - k}} \quad (43)$$

where n is the number of degrees of freedom, $k=2$ is the number of dependent model factors. The standard errors of the elements of A are given by the diagonal elements of ΔA and d is the original zonal velocity from the Argo floats. The degree of freedom is the number of the data used, assuming each measurement to be independent. The explained variance of the harmonic fit is then defined by

$$Ve = \frac{Var(d) - Var(d - d_m)}{Var(d)} \quad (44)$$

where Var is the sample variance.

For comparison, we first calculate the zonally and temporally averaged square of the zonal velocity for each A_h in the forcing case “Equator” in the simulation without mean flow (similar to Fig. 3.8 for the case “Full”), then normalize them by the area integration between $1^\circ S$ and $1^\circ N$ for each A_h , so that the area under each curve between $1^\circ S$ and $1^\circ N$ is the same. The

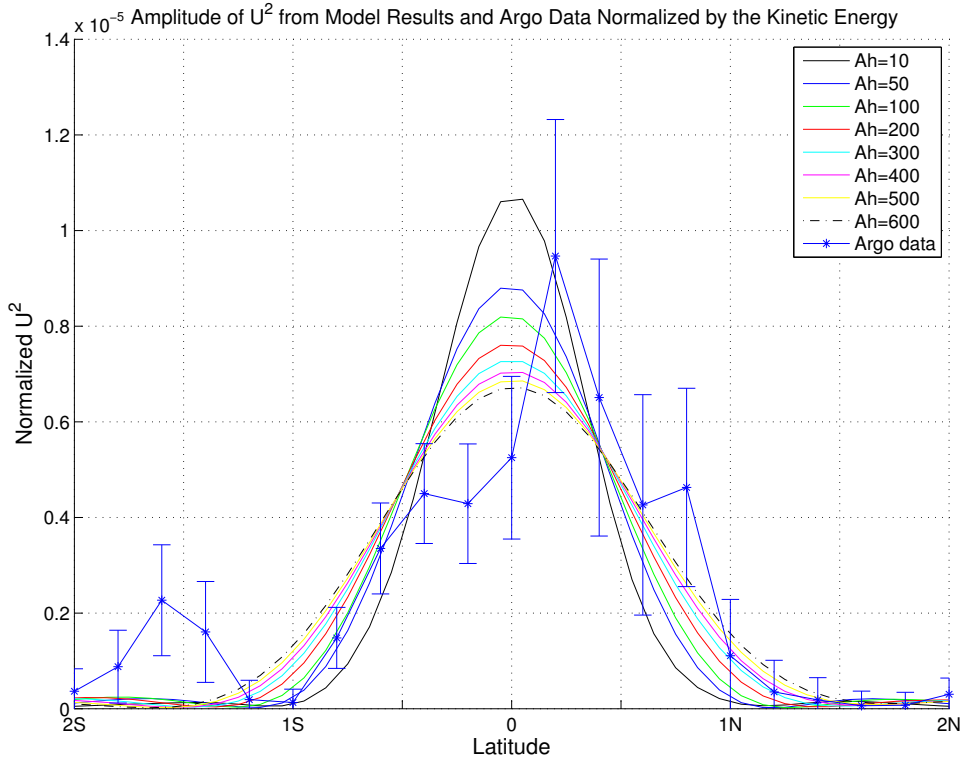


Figure. 3.25 | The same as in Fig. 3.24, except that the result for the forcing case “Equator” in the simulation with mean flow is used. Note that the zonal velocities squared from both model and Argo float data, together with the error bars, are normalized to give the same area under each curve between $1^\circ S$ and $1^\circ N$. The unit of A_h is m^2/s .

result is plotted in Fig. 3.24, together with the meridional profile obtained from the harmonic fit (Fig. 3.23); note that the profile from the Argo float data is normalized in the same way. As we see from the figure, on the southern side of the equator, the observation agrees very well with the model response for A_h between 50 and 200 m^2/s within the latitude range from $1^\circ S$ to $0.5^\circ S$. All the model cases fail to simulate the peak between $2^\circ S$ and $1.5^\circ S$. On the northern side of the equator, even the largest value of A_h cannot agree with the observation within the latitude range from $0.2^\circ N$ to $1^\circ N$. This is a consequence of the weakening dependence of the simulated EDJ width to large values of A_h as mentioned when discussing Fig. 3.10. However, if we take the error bars into account, except at $0.8^\circ N$, all the curves lie within the error bars, allowing a wide range of eddy viscosities A_h to satisfy the observed width. As a conclusion, taking into account the asymmetric structure about the equator of the observed data, this result is in a good agreement with the previously discussed A_h value of 300 m^2/s (see discussion on Fig. 3.10), which is sufficient to account for the observed cross-equatorial width of the EDJs.

Comparing the profile of the harmonic fit amplitude with the profiles from the model sim-

ulation with mean flow for the case “Equator” (Fig. 3.25), we see a very similar structure as before. However, on the northern side of the equator, the model results tend to agree with the observation better than in Fig. 3.24. This is a consequence of the widening caused by the mean flow as discussed in Fig. 3.19. As a result, at $0.8^\circ N$, the curves for $A_h = 500$ and $600 \text{ m}^2/\text{s}$ lay within the range of the error bar at this latitude, this improves the compatibility between the model simulation and the observation.

3.2.2 Root Mean Square Comparison

After the profile comparison, a calculation of the root-mean-square difference (RMS) between the amplitude of the zonal velocity from the Argo float and the model is designed. As discussed before, the eddy viscosity of $300 \text{ m}^2/\text{s}$ is a good estimation to account for the observed width of the Atlantic EDJs. We therefore use the simulation result for $A_h = 300 \text{ m}^2/\text{s}$ of the case “Equator” in both runs with/without mean flow to calculate the RMS with the Argo float data. For a precise calculation, the RMS is designed in a point-to-point sense, which means that the square of the difference between the Argo float data and the model output data is computed at each measuring location and time.

Prior to the calculation, several preparation steps need to be done. First of all, the time series of the model simulation is not initialized referring to any real time point, it starts from 0 s and increases by $\Delta t \text{ seconds}$ in each time step to the end of the model run. Therefore, it is essential to match the model time series with a real time series. Given the fact that both of the model simulation and the observed Atlantic EDJs share the gravest basin mode period $T_B = 1670 \text{ days}$, we could refer the model time series to the time series of the Argo float data by matching the phase of the model with the phase of the harmonic fit to the zonal velocity from the Argo float data along the equator. Practically, this can be done by searching for the model time step, at which the phase of the modelled zonal velocity at the equator is the same as the phase of the beginning point of the harmonic fit to the zonal velocity along the equator.

Fig. 3.26 shows the 1670-day harmonic fit for the equatorial bin of the Argo float data, together with the fitted model solution. The equatorial bin extends from $30^\circ W$ to $15^\circ W$ and extends 0.25° either side of the equator; also, the harmonic fit is exactly the same as in Fig. 3.22. The model solution is taken at $23^\circ W$ at the equator in the simulation without mean flow. Previously, the zonal velocity between $30^\circ W$ and $15^\circ W$ was binned in order to create a harmonic fit. We therefore choose $23^\circ W$ as the longitude where the phase of the zonal velocity from the model solution is to be matched with the corresponding phase of the Argo float data.

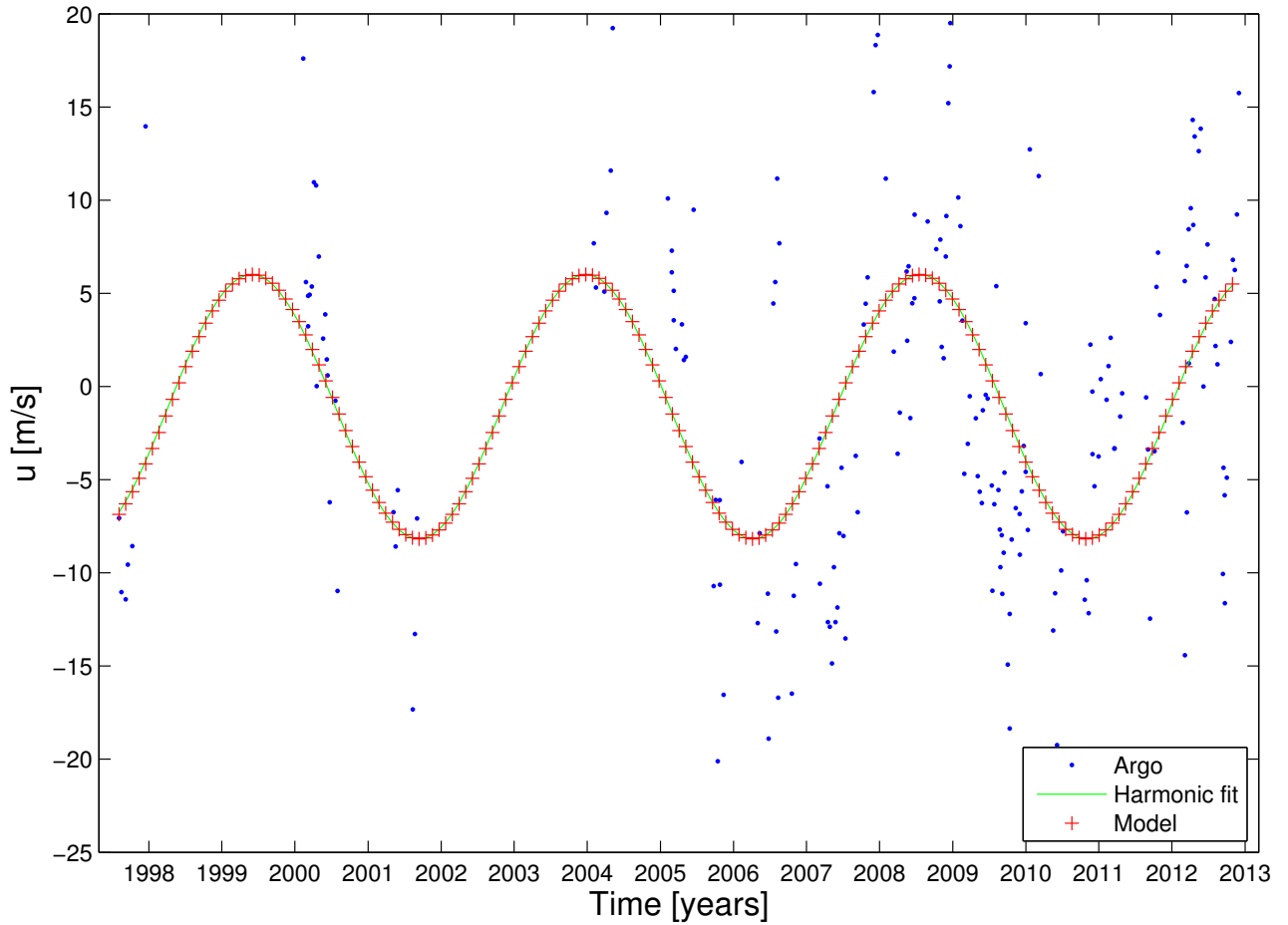


Figure. 3.26 | The 1670-day harmonic fit for the equatorial bin (centred at 0° latitude), together with the fitted model solution. The dots are the sorted zonal velocity from the Argo float data in cm/s, the green curve is the corresponding harmonic fit, and the red plus sign represents the zonal velocity at $23^\circ W$ at the equator in the simulation without mean flow. Note that the amplitude of the zonal velocity from the model is given by the amplitude of the harmonic fit along the equator; and that the Argo float data used here and the corresponding harmonic fit is the same as in Fig. 3.22.

Also, the amplitude of the model solution is first normalized by the maximum eastward zonal velocity at this location, then multiplied by the amplitude of the corresponding harmonic fit. As we see, the zonal velocity at $23^\circ W$ at the equator from the model shares exactly the same real time series with the fit to the Argo float data along the equator. Therefore, we refer the starting time step of the matched model result at $23^\circ W$ at the equator shown in Fig. 3.26 to Aug 5 1997, and we choose the model data starting on this day for comparison with the Argo float data. However, please be aware that the phase of the model itself varies with latitude (Fig. 3.12), whereas this fitted model solution is only the best fit of the model phase at $23^\circ W$.

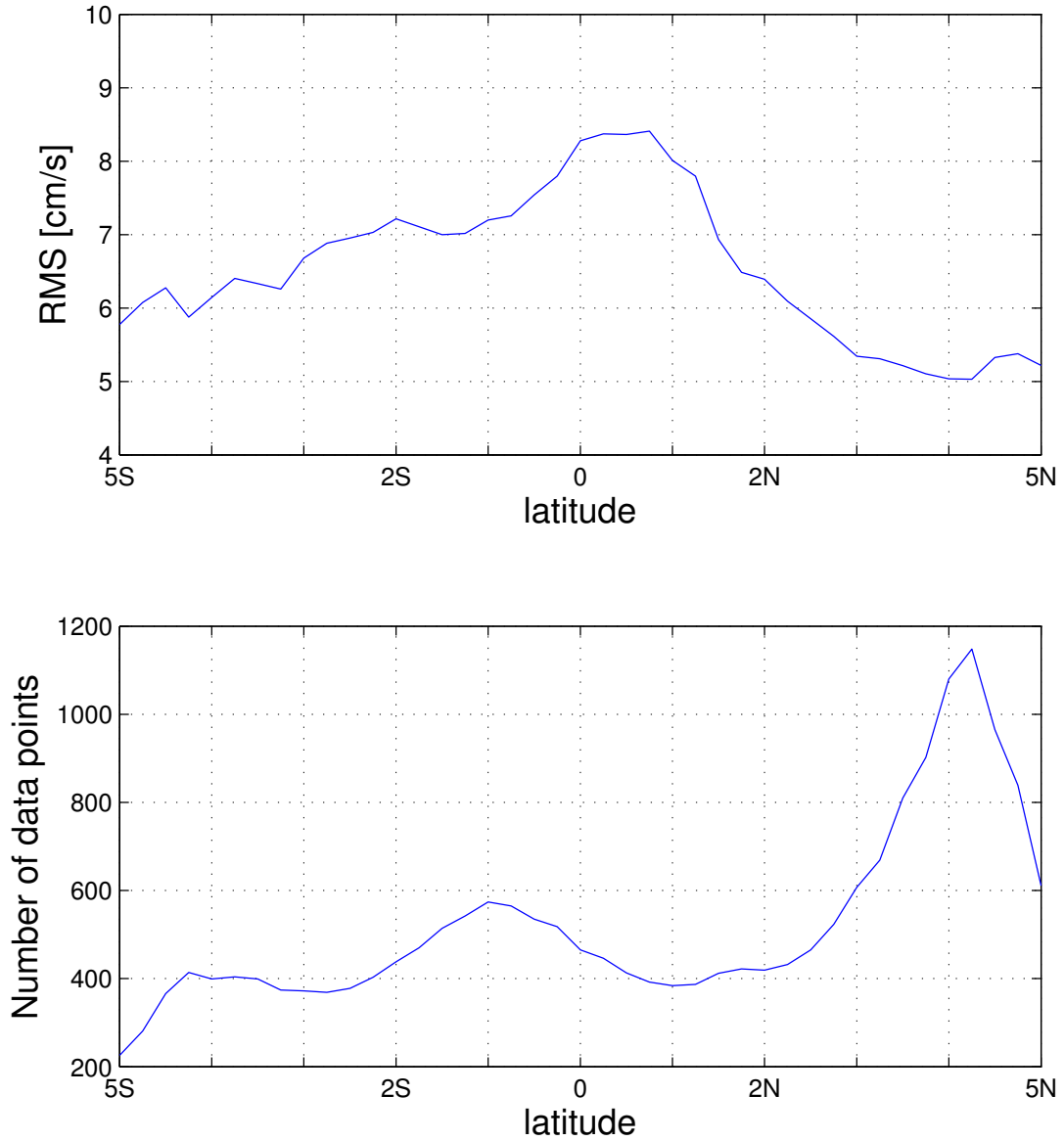


Figure. 3.27 | The root mean square difference between the zonal velocities from the Argo floats and the model simulation without mean flow (upper panel), and the number of available Argo float data (lower panel) as a function of latitude. The square of the difference is first calculated “point-to-point”, then the square root is taken after averaging the square of the difference within each latitude bin.

at the equator to the Argo float data.

Secondly, although the information about the measuring location is recorded in the Argo float data, the data are not saved in the same format as the model output data. For this reason, we re-construct the zonal velocity from the Argo float data according to the grid used by the model output data to simplify the calculation of the RMS. This is done by allocating the Argo float data to the closest location in the model grid and the closest time in the model time series

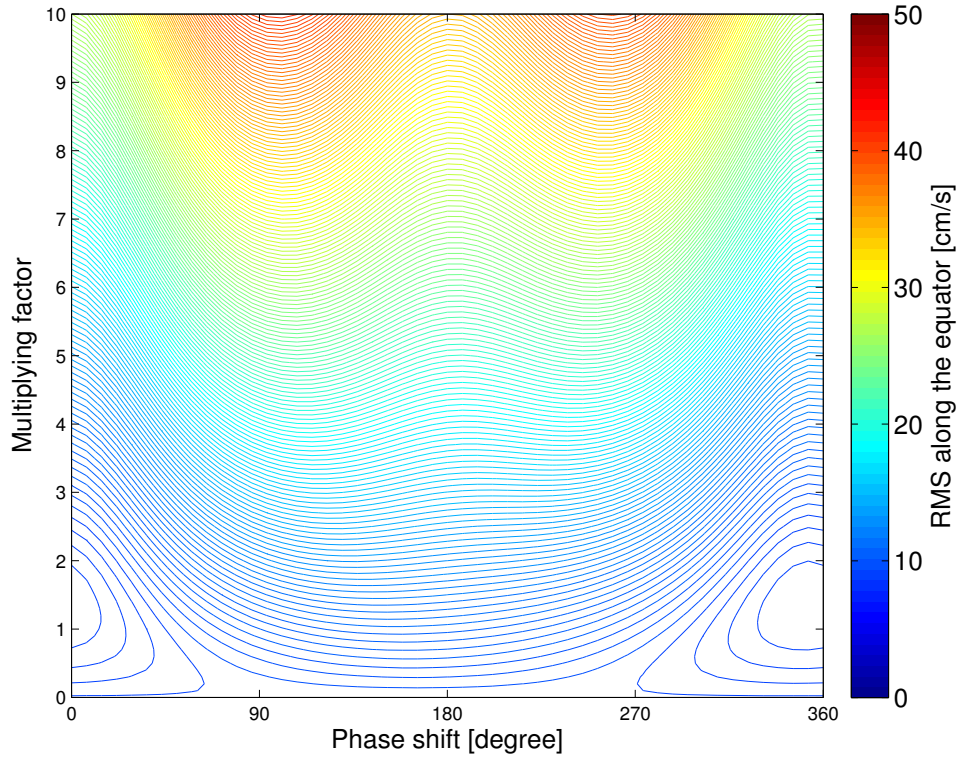


Figure. 3.28 | The optimization calculation of minimizing the RMS at the equator. This is done by shifting the phase of the model solution from 0° to 360° , and simultaneously magnifying the model solution by a dimensionless factor varying from 0 to 10, before the point-to-point calculation of the difference between the zonal velocities from Argo floats and model within the equatorial bin.

designated in Fig. 3.26. Doing so gives us a 3-dimensional matrix of the zonal velocity from the Argo float data in exactly the same size of the model output data. The locations and time steps at which no zonal velocity is measured by the Argo float data are filled with missing values, and have no influence on the RMS calculation at all.

Following the presetting above, we keep the maximum amplitude of the model solution given by the amplitude of the harmonic fit to the zonal velocity along the equator, and restrict the application of both Argo data and model data still within the longitude band between $30^\circ W$ and $15^\circ W$. Fig. 3.27 shows the root mean square difference between the zonal velocities from the Argo floats and the model simulation without mean flow as a function of latitude. The square of the difference between the Argo data and model data is first calculated at each location and time, the result is binned into overlapping latitude bands of width 1.5° centred on a 0.25° grid, then the square root is taken after the square of the difference is averaged within each latitude bin. Note that the equatorial bin used for the RMS calculation is broader than

that used for the harmonic fit, for the purpose of increasing the number of the Argo float data. As shown in the figure, the RMS is the largest at the equator, and decreases with latitude on either side of the equator. This is not a surprising feature if we look back at Fig. 3.24, in which the amplitude of the harmonic fit deviates from that of the model at many places between $0.75^\circ S$ and $0.75^\circ N$. Between $2.5^\circ S$ and $1^\circ S$, the RMS is also relatively high, this may be related to the small peak in the harmonic fit amplitude at about $1.5^\circ S$. Between $3^\circ N$ and $5^\circ N$, the number of the Argo float data is larger, while the RMS is smaller than at any other latitude.

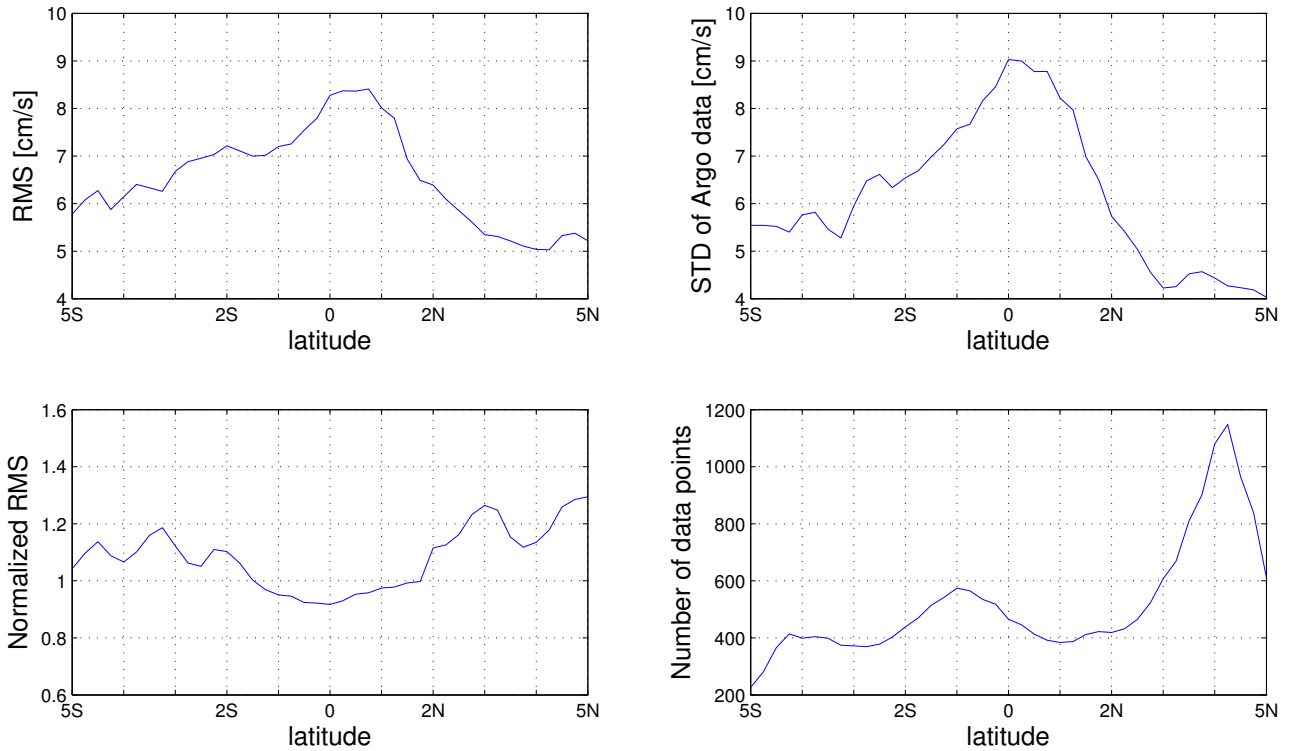


Figure. 3.29 | The same RMS as in Fig. 3.27 (upper left), the standard deviation of the Argo float data in each latitude bin (upper right), the RMS divided by the standard deviation at each latitude (lower left), and the number of the Argo float data in each latitude bin (lower right).

Based on the RMS result shown in Fig. 3.27, a further optimizing attempt is made to reduce the RMS at the equator. This is done by artificially shifting the phase of the model solution forward from 0° to 360° , and simultaneously multiplying the model solution by a dimensionless factor varying from 0 to 10, before the point-to-point calculation of the difference between the zonal velocities from the Argo float and the model within the equatorial bin. Fig. 3.28 shows the result of the optimization at the equator as a function of the phase shift and the multiplying

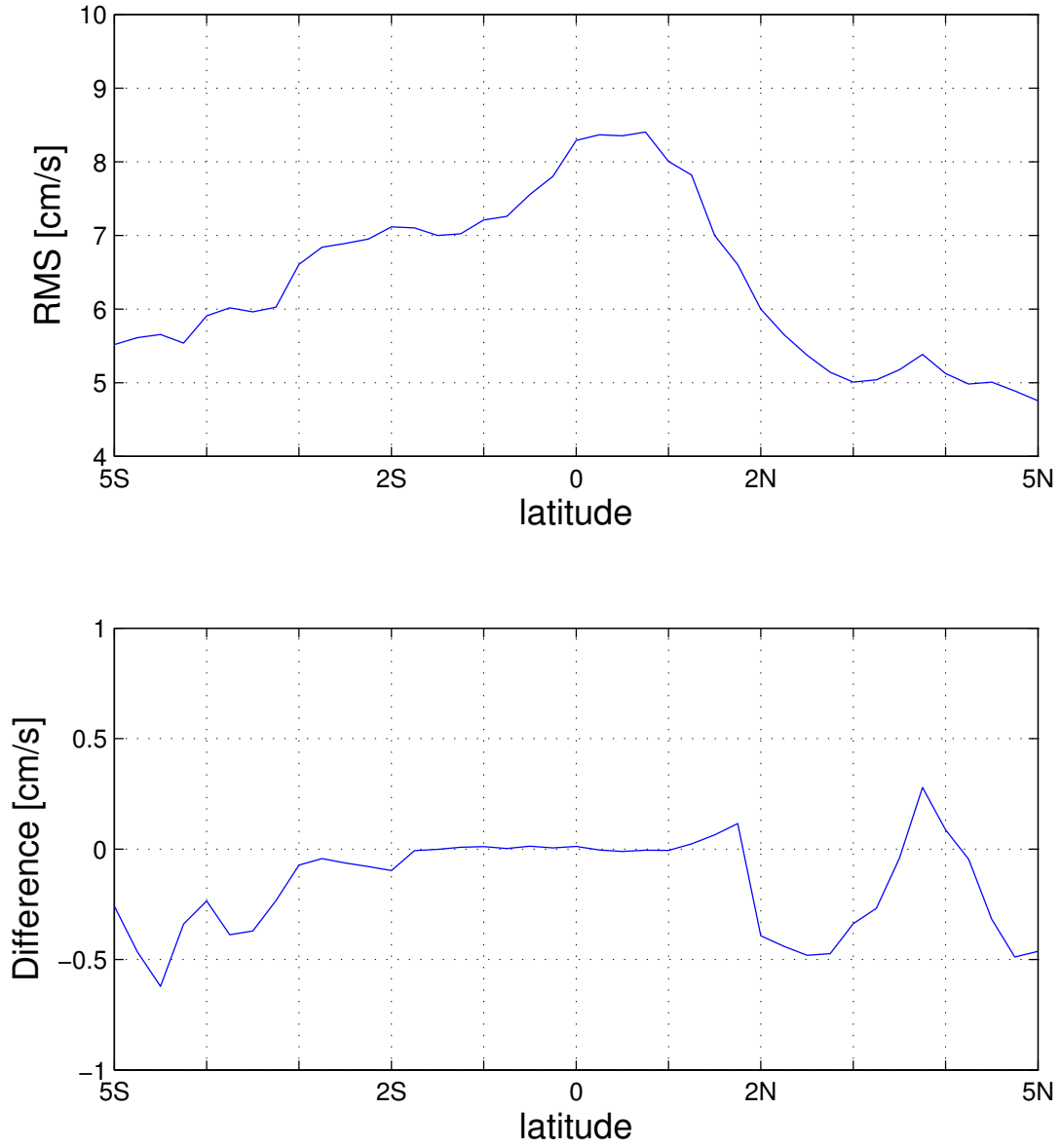


Figure. 3.30 | The RMS for the simulation with mean flow (upper panel), and the difference of the RMS between the the simulation with/without mean flow (lower panel), as a function of latitude. In the lower panel, positive values mean the the RMS between Argo float data and the model with mean flow is larger than that between Argo data and the model without mean flow.

factor of the model solution. The contour lines represents the resulting RMS at the equator, with a minimum located at a phase shift of 0° and multiplying factor of 1.3 in respect to the model solution in Fig. 3.26. This 0° phase shift verifies our choice of the zonal velocity at $23^\circ W$ at the equator when matching the phase of the model with the phase of the harmonic fit to the Argo float data. However, applying this equatorially optimized phase and amplitude to the model, we compute the RMS again as a function of latitude in the same way as before

(not shown here). It shows a decrease of the RMS at the equator by only about 0.03 cm/s but an increase of the RMS away from the equator by about 0.5 cm/s . Therefore, we do not apply this optimization to the RMS calculation for the simulation without mean flow.

In the lower left plot of Fig. 3.29, the RMS is divided by the standard deviation (upper right) of each latitude bin. In general, the normalized RMS is close to 1 near the equator, and increase to about 1.2 and 1.4 at $5^\circ S$ and $5^\circ N$, respectively. This implies a close relation between the large variability of the Argo float data and the large values of RMS near the equator.

For the RMS comparison for the simulation with mean flow, we follow the same procedure: first the model data is fitted to the harmonic fit of the Argo float data by matching the phase of the zonal velocities at the equator (the same as Fig. 3.26); then the argo flow data is reconstructed in the format of the model data; in the end the RMS is calculated as a function of latitude. The optimizing attempt (not shown) in this simulation also failed to decrease the overall RMS.

Fig. 3.30 shows the RMS between the Argo float data and the model simulation with mean flow, and the difference in the RMS between these two simulations. The result is very similar to Fig. 3.29 (upper left), with large values around the equator and decreasing with latitude. Looking at the difference in the RMS calculation, we only see relatively large difference at latitudes higher than 1.75° on both sides of the equator; the negative difference means a smaller RMS in the model simulation with mean flow. This result then reflects that at higher latitudes, the model simulation with mean flow is more compatible with the observations than the simulation without mean flow, although this improvement in the amplitude by the barotropic mean flow is very small, less than 1 cm/s .

4 Summary and Discussion

A linear shallow water model is used to simulate a forced, dissipative equatorial basin mode for a high-order baroclinic vertical normal mode. As discussed by many authors (*Johnson and Zhang, 2003*; *D’Orgeville et al., 2007*; *Brandt et al., 2011*), the Atlantic equatorial deep jets share a great similarity with the gravest equatorial basin mode. Therefore, this model is taken as a simple representation of the equatorial deep jets (EDJs). As demonstrated in Fig. 3.10, the existence of the lateral mixing of momentum with eddy viscosity results in an increase of the cross-equatorial width of the simulated EDJs. The widening of the EDJs by the lateral mixing of momentum could be responsible for the enhanced cross-equatorial width of the observed EDJs compared to that implied by linear inviscid theory. The enhanced width has been noted by *Johnson and Zhang (2003)* in the Atlantic Ocean and by *Muench et al. (1994)* in the Pacific Ocean. The lateral mixing of momentum also leads to a reduction in the strength of the zonal velocity along the equator (Fig. 3.11). The corresponding mechanism can be understood as that at the equator, the large zonal scale zonal flows are in geostrophic balance, in the absence of diapycnal mixing to remove the density anomalies, the reduction in the zonal velocity due to lateral mixing must be compensated by a weaker density gradient, hence a broader jet. The influence of the different forcing locations on the width and strength of the EDJs has been investigated. It is found that forcing in the centre of the basin is probably the most efficient way of exciting a basin mode.

Through the comparison between the width implied by the inviscid theory and the width in the simulation case with forcing zonally uniform over the equator, but meridionally confined within an equatorial Rossby radius of deformation either side of the equator (forcing case “Equator”), a value of the eddy viscosity $A_h = 300 \text{ m}^2/\text{s}$ is estimated to account for the observed cross-equatorial width of the EDJs. This value of A_h has been confirmed to be sufficient by comparison of the meridional profiles of the zonal velocity between the simulations and the Argo float data, and it is consistent with the value of $400 \text{ m}^2/\text{s}$ suggested by *Brandt et al. (2011)* to close the oxygen budget along the equator. Furthermore, the root mean square difference (RMS) between the zonal velocity from the Argo float data and the model simulation is calculated. It is found that the RMS is the largest near the equator and decreases with latitude either side of the equator (Fig. 3.29). The large value of the RMS near the equator may arise from both the large variability in the zonal velocity from the Argo data and the northward bias in the observed zonal velocity near the equator, a feature that is not found in the model results

(Fig. 3.24).

A further attempt was made to examine the influence of a background barotropic mean flow on the horizontal structure of the simulated EDJs. The cross-equatorial width of the simulated EDJs for a given forcing case is generally larger in the simulation with mean flow than in the simulation without mean flow. As a result, on the northern side of the equator, the model simulation with mean flow is more compatible with the Argo float data in the comparison of the meridional profiles of the zonal velocity (see discussion in Fig. 3.24). A value of $300 \text{ m}^2/\text{s}$ is still a reasonable estimation for the eddy viscosity A_h ; also, for the RMS calculation, the simulation with mean flow shows a better consistency with the Argo float data at latitudes higher than 2.5° (Fig. 3.30). Taken together, the results of both simulations with/without mean flow are consistent with each other; and the implementation of the background barotropic mean flow improves the consistency of the modelled data with the observational data, especially at latitudes higher than 2.5° either side of the equator.

Based on the results, we believe that further work is required to test the importance of other processes for the EDJs, for example, a varying lateral eddy viscosity, A_h , with latitude. As discussed by [Greatbatch et al. \(2012\)](#), the flanking jets near $2^\circ N$ and $2^\circ S$ may influence the EDJs by altering A_h , and in reality, it is also possible that the lateral eddy viscosity varies spatially with the background mean flow. Also, a more realistic coastline may result in a different wave structure at the boundaries, although we did not use data (model or observations) close to the boundaries. In addition, as shown in Fig. 3.23, the amplitude of the northward biased maximum zonal velocity decreased in the updated Argo float data, compared to Fig. 5 of [Greatbatch et al. \(2012\)](#). It is possible that a longer measurement period and a more complete spatial coverage of the observational data would reduce the uncertainties in the calculation of the EDJs and provide a more accurate comparison between the model simulation and the observations.

Note that in order to counter the dissipation by the lateral mixing of momentum, a resonant forcing with the period of the gravest equatorial basin mode $T_0 = 1670 \text{ days}$ was applied. Since the model is linear, the amplitude of the forcing is just an arbitrary choice. For example, the amplitude of the forcing used in this work is too large when the resulting amplitude of the zonal velocity in the model simulation is up to 20 m/s . Therefore, the amplitude can be reduced in the future studies. Besides, in order to keep the gravity wave speed $c = 0.17 \text{ m/s}$, the equivalent depth $H_e = 2.9 \times 10^{-3} \text{ m}$ was used. This condition, in turn, gives a very small isopycnal displacement, even though the zonal velocity is unrealistically large. Although the isopycnal

displacement is not the main concern of this work, one can still obtain a relatively realistic isopycnal displacement for a given velocity by scaling η from our simulation in a reduced-gravity sense, in which a layer thickness H' should be pre-defined, and the corresponding reduced gravity g' can be calculated by $g' = c^2/H'$. The “realistic” isopycnal displacement η' is then given by $\eta' = \eta H'/H_e$. This is illustrated for the case of the analytical solution of the equatorial basin mode (Fig. 3.1 and 3.2).

Nevertheless, the EDJs show a downward phase propagation (Fig. 1.1a), associated with vertical energy transfer. For this reason, a equatorial basin mode cannot exactly represent the EDJs. In reality, there must be a set of different vertical modes, and the energy is transferred between these modes. These features should be further examined in 3-dimensional models. However, the existence of different vertical modes should not change the fact that the simple mechanism concerning the role of the lateral mixing of momentum is still applicable. Therefore, the results shown before are still valid.

5 Acknowledgement

I am grateful to Prof. Richard Greatbatch and Prof. Peter Brandt for the supervision of my master program and for the helpful suggestions during our discussions. And I would like to thank Martin Claus for patiently introducing me the shallow water model and answering all the questions, also thank Sven-Helge Didwischus for helping me processing the Argo float data, and Hui Ding for answering my general questions, also Rafael Abel for the help in Latex and advises about writing, as well as the Theory and Modelling department for the warm and nice atmosphere. This study used the data of YoMaHa'07, [Lebedev et al. \(2007\)](#) dataset of velocities derived from Argo float trajectories and provided by APDRC/IPRC.

Special thanks to my parents for their generous support of my master study in Germany.

Erklärung

Ich versichere, dass ich die Arbeit selbstständig verfasst und keine anderen als die angegebenen Hilfsmittel insbesondere keine im Quellenverzeichnis nicht genannten Internet-Quellen - benutzt habe, die Arbeit vorher nicht in einem anderen Prüfungsverfahren eingereicht habe und die eingereichte schriftliche Fassung der auf dem elektronischen Speichermedium entspricht. Ich erkläre mich auerdem damit einverstanden, dass ein Exemplar der Abschlussarbeit der Institutsbibliothek zur Verfügung gestellt wird. Ich stimme einer Veröffentlichung der Arbeit zu. Weiterhin versichere ich, dass diese Arbeit noch nicht als Abschlussarbeit an anderer Stelle vorgelegen hat.

References

- Brandt, P., V. Hormann, B. Bourlès, J. Fischer, F. a. Schott, L. Stramma, and M. Dengler (2008), Oxygen tongues and zonal currents in the equatorial Atlantic, *Journal of Geophysical Research*, *113*(C4), C04,012, doi:10.1029/2007JC004435. [10](#), [11](#), [32](#)
- Brandt, P., A. Funk, V. Hormann, M. Dengler, R. J. Greatbatch, and J. M. Toole (2011), Interannual atmospheric variability forced by the deep equatorial Atlantic Ocean., *Nature*, *473*(7348), 497–500, doi:10.1038/nature10013. [5](#), [7](#), [10](#), [19](#), [20](#), [44](#), [54](#)
- Brandt, P., et al. (2012), Ventilation of the equatorial Atlantic by the equatorial deep jets, *Journal of Geophysical Research*, *117*(C12), C12,015, doi:10.1029/2012JC008118. [5](#), [6](#), [7](#)
- Bunge, L., C. Provost, B. L. Hua, and A. Kartavtseff (2008), Variability at Intermediate Depths at the Equator in the Atlantic Ocean in 200006: Annual Cycle, Equatorial Deep Jets, and Intraseasonal Meridional Velocity Fluctuations, *Journal of Physical Oceanography*, *38*(8), 1794–1806, doi:10.1175/2008JPO3781.1. [5](#)
- Cane, M., and D. Moore (1981), A Note on Low-Frequency Equatorial Basin Modes, *Journal of . . . , II*, 1578–1584. [10](#), [22](#), [23](#), [35](#)
- Dengler, M., and D. Quadfasel (2002), Equatorial deep jets and abyssal mixing in the Indian Ocean, *Journal of Physical Oceanography*, *32*(4), 1165–1180. [11](#)
- D’Orgeville, M., B. Hua, and H. Sasaki (2007), Equatorial deep jets triggered by a large vertical scale variability within the western boundary layer, *Journal of Marine Research*, *25*(1), 1–25, doi:10.1357/002224007780388720. [7](#), [10](#), [54](#)
- Eden, C., and M. Dengler (2008), Stacked jets in the deep equatorial Atlantic Ocean, *Journal of Geophysical Research*, *113*(C4), C04,003, doi:10.1029/2007JC004298. [5](#), [6](#), [7](#)
- Eriksen, C. (1981), Deep currents and their interpretation as equatorial waves in the western Pacific Ocean, *Journal of Physical Oceanography*, *11*(1), 48–70, doi:http://dx.doi.org/10.1175/1520-0485(1981)011<0048:DCATIA>2.0.CO;2. [5](#)
- Eriksen, C. C. (1982), Geostrophic Equatorial Deep Jets, *J. Mar. Res.*, *40*, 143–157. [5](#)
- Fruman, M. D., B. L. Hua, and R. Schopp (2009), Equatorial Zonal Jet Formation through the Barotropic Instability of Low-Frequency Mixed RossbyGravity Waves, Equilibration by Inertial Instability, and Transition to Superrotation, *Journal of the Atmospheric Sciences*, *66*(9), 2600–2619, doi:10.1175/2009JAS2913.1. [7](#)
- Gerkema, T., L. R. M. Maas, and H. van Haren (2013), A Note on the Role of Mean Flows in Doppler-Shifted Frequencies, *Journal of Physical Oceanography*, *43*(2), 432–441, doi:10.1175/JPO-D-12-090.1. [35](#)
- Gill, A. (1982), *Atmosphere-Ocean Dynamics*, 662 pp., Academic Press. [8](#), [28](#)

- Gill, A., and A. Clarke (1974), Wind-induced upwelling, coastal currents and sea-level changes, *Deep Sea Research and Oceanographic Abstracts*, 21(November 1973), 325–345. [8](#)
- Greatbatch, R. J., P. Brandt, M. Claus, S.-H. Didwischus, and Y. Fu (2012), On the Width of the Equatorial Deep Jets, *Journal of Physical Oceanography*, 42(10), 1729–1740, doi:10.1175/JPO-D-11-0238.1. [11](#), [12](#), [28](#), [32](#), [34](#), [43](#), [55](#)
- Hayes, S., and H. Milburn (1980), On the Vertical Structure of Velocity in the Eastern Equatorial Pacific, *Journal of Physical Oceanography*, 10(4), 633–634. [5](#)
- Hua, B., M. D’orgeville, M. Fruman, C. Menesguen, R. Schopp, P. Klein, and H. Sasaki (2008), Destabilization of mixed Rossby gravity waves and the formation of equatorial zonal jets, *Journal of Fluid ...*, 610(September), 311–341, doi:10.1017/S0022112008002656. [7](#)
- Hua, B. L., D. W. Moore, and S. L. Gentil (1997), Inertial nonlinear equilibration of equatorial flows, *Journal of Fluid Mechanics*, 331, 345–371, doi:10.1017/S0022112096004016. [7](#)
- Johnson, G., and D. Zhang (2003), Structure of the Atlantic Ocean Equatorial Deep Jets*, *Journal of physical oceanography*, pp. 600–609. [5](#), [10](#), [30](#), [54](#)
- Lebedev, K. V., H. Yoshinari, N. A. Maximenko, and P. W. Hacker (2007), YoMaHa07: Velocity data assessed from trajectories of Argo floats at parking level and at the sea surface. [19](#), [57](#)
- Leetmaa, A., and P. Spain (1981), Results from a Velocity Transect along the Equator from 125 to 159 W, *Journal of Physical Oceanography*, 11(7), 1030–1033. [5](#)
- Luyten, J. R., and J. C. Swallow (1976), Equatorial Undercurrents, in *Deep Sea Research*, vol. 23, pp. 999–1001, Elsevier. [5](#)
- Muench, J., E. Kunze, and E. Firing (1994), The potential vorticity structure of equatorial deep jets, *Journal of physical oceanography*, 24, 418–428. [5](#), [54](#)
- Ponte, R., and J. Luyten (1990), Deep Velocity Measurements in the Western Equatorial Indian Ocean, *Journal of physical oceanography*, 20(1), 44–52. [5](#)
- Sadourny, R. (1975), The dynamics of finite-difference models of the shallow-water equations, *Journal of the Atmospheric Sciences*, 32. [18](#)
- Schopf, P., D. Anderson, and R. Smith (1981), Beta-dispersion of low-frequency Rossby waves, *Dynamics of Atmospheres and ...*, 5, 187–214. [35](#)
- Yamagata, T., and S. Philander (1985), The role of damped equatorial waves in the oceanic response to winds, *Journal of the Oceanographical Society of ...*, 41(parameter 7). [10](#)
- Yang, H., and Z. Liu (2003), Basin Modes in a Tropical-Extratropical Basin*, *Journal of physical oceanography*, pp. 2751–2763. [14](#)